arXiv:0709.1926v1 [astro-ph] 12 Sep 2007

Distances to Galactic high-velocity clouds. I. Cohen Stream, complex GCP, cloud g1 [1]

B.P. Wakker[1], D.G. York[2], R. Wilhelm[3], J.C. Barentine[4], P. Richter[5], T.C. Beers[6], Ž. Ivezić[7], J.C. Howk[8]

ABSTRACT

The high- and intermediate-velocity interstellar clouds (HVCs/IVCs) are tracers of energetic processes in and around the Milky Way. Clouds with near-solar metallicity about one kpc above the disk trace the circulation of material between disk and halo (the Galactic Fountain). The Magellanic Stream consists of gas tidally extracted from the SMC, tracing the dark matter potential of the Milky Way. Several other HVCs have low-metallicity and appear to trace the continuing accretion of infalling intergalactic gas. These assertions are supported by the metallicities (0.1 to 1 solar) measured for about ten clouds in the past decade. Direct measurements of distances to HVCs have remained elusive, however. In this paper we present four new distance brackets, using VLT observations of interstellar Ca II H and K absorption toward distant Galactic halo stars. We derive distance brackets of 5.0 to 11.7 kpc for the Cohen Stream (likely to be an infalling low-metallicity cloud), 9.8 to 15.1 kpc for complex GCP (also known as the Smith Cloud or HVC 40−15+100 and with still unknown origin), 1.0 to

[1]Department of Astronomy, University of Wisconsin, Madison, WI 53706; wakker@astro.wisc.edu

[2]Astronomy & Astrophysics Center, University of Chicago, Chicago, IL 60637; don@oddjob.uchicago.edu

[3]Dept. of Physics & Astronomy, Texas Tech University, Lubbock TX 79409; ron.wilhelm@ttu.edu

[4]Dept. of Astronomy, Univ. of Texas, Austin TX 78712 and Apache Point Observatory, Sunspot, NM 88349; jcb@astro.as.utexas.edu

[5]Institut für Physik, Universität Potsdam, Am Neuen Palais 10, 14469 Potsdam, Germany; prichter@astro.physik.uni-potsdam.de

[6]Department of Physics and Astronomy, CSCE: Center for the Study of Cosmic Evolution and JINA: Joint Institute for Nuclear Astrophysics, Michiga n State University, E. Lansing, MI 48824, USA; beers@pa.msu.edu

[7]Dept. of Astronomy, University of Washington, Box 351580, Seattle, WA 98195; ivezic@astro.washington.edu

[8]Dept. of Physics, University of Notre Dame, Notre Dame, IN 46556; jhowk@nd.edu

2.7 kpc for an IVC that appears associated with the return flow of the Fountain in the Perseus Arm, and 1.8 to 3.8 kpc for cloud g1, which appears to be in the outflow phase of the Fountain. Our measurements further demonstrate that the Milky Way is accreting substantial amounts of gaseous material, which influences the Galaxy's current and future dynamical and chemical evolution.

Subject headings: ISM: clouds, Galaxy: halo, Galaxy: high-velocity clouds, stars: distances, stars: horizontal branch

1. Introduction

The evolution of galaxies is strongly driven by the gas in the interstellar medium. High- and low-mass stars form from gas in the disk and put back energy into the gas. Some gas escapes from the disk, forming a hot atmosphere. As this gas cools and rains back it forms a "Galactic Fountain". The hot atmosphere has been called the "Galactic Corona", and it extends up to 10 kpc above the Galactic disk. There is also infall of new material that provides fuel for galaxy growth. This material can originate in small satellite galaxies, as gas tidally pulled out of passing galaxies, and from more pristine intergalactic gas. The cool clouds that fall in would be embedded in (or condense out of) a much more extended (100–200 kpc radius) hot Corona, different from the one formed by star-formation processes. Indirect evidence for infalling gas is provided by two arguments (Chiappini et al. 2001). First, at the current rate of star formation, all of the ISM would be turned into gas within about a Gyr. Second, the narrowness of the distribution of metallicities of long-lived stars is best explained if the metallicity of the ISM remains more or less constant over a Hubble time, which happens if there is an inflow of low-metallicity material from outside. The predicted inflow rate decreases with time and at present is on the order of 1 $M_\odot\,yr^{-1}$.

Direct observational evidence for the processes mentioned above is provided by the high-velocity clouds (see reviews by Wakker & van Woerden 1997; Richter 2006). They are defined observationally as clouds with velocities that are incompatible with differential galactic rotation. In practice this means $|v_{\rm LSR}|$>50 km s^{-1}. Historically, such gas has been divided into the high-velocity clouds (HVCs), having $|v_{\rm LSR}|$>90 or >100 km s^{-1}, and the intermediate-velocity clouds (IVCs), with $|v_{\rm LSR}|$=50 to 100 km s^{-1}. They have been mapped extensively

[1]Based on observations carried out at the European Southern Observatory (ESO), La Silla, under prog. ID No. 077.B-0359 (PI: P. Richter) with the UVES spectrograph at the ESO Very Large Telescope, Paranal, Chile.

in 21-cm emission (see Hulsbosch & Wakker 1988; Wakker & van Woerden 1991; Hartmann & Burton 1997; Morras et al. 2000; Kalberla et al. 2005). The different origins of different clouds can be determined by measuring their metallicities and distances. Solar metallicity clouds near the disk trace the Galactic Fountain. Distant (>5 kpc), low-metallicity (0.01-0.2 solar) clouds trace infall. Long streams with intermediate metallicity are likely to be tidal. Intrinsic metallicities (Z) have been determined for a few HVCs (see van Woerden & Wakker 2004 for a summary). The best values are $Z{\sim}0.15$ times solar for complex C (Wakker et al. 1999; Richter et al. 2001; Tripp et al. 2003; Sembach et al. 2004), while clouds in the Magellanic Stream have SMC-like metallicity ($\sim$ 0.25 solar; Lu et al. 1998; Gibson et al. 2000). Van Woerden & Wakker (2004) list approximate values for a total of eight HVCs, ranging from 0.1 to 1 times solar. In contrast, the intermediate-velocity clouds are usually found to have near-solar metallicity (Wakker 2001; Richter et al. 2001).

The main unknown for the HVCs remains their distances. If we knew these, we could derive empirical (rather than theoretical) estimates for the rate of accretion of low-metallicity (0.01–0.1 solar) gas, the rate of circulation of gas between disk and halo,, and the mass of tidal material around the Milky Way. Furthermore, HVCs could be used to calibrate the fraction of ionizing photons escaping the Milky Way disk, as many HVCs are seen in Hα emission (see Bland-Hawthorn & Maloney 1999).

Although the first paper on determining distances to HVCs was published four decades ago (Prata & Wallerstein 1967), progress has been slow. Wakker (2001) summarized the state of knowledge a few years back. It is clear that distances to several IVCs are on the order of 1–2 kpc. However, for HVCs Wakker (2001) only lists lower limits of 6 kpc to complex C ($v_{\rm LSR}{\sim}-150$ km s^{-1}), 5 kpc to complex H ($v_{\rm LSR}{\sim}-180$ km s^{-1}), and 0.3 kpc to the Anti-Center clouds (clouds with $v_{\rm LSR}{\sim}-250$ km s^{-1} and $v_{\rm LSR}{\sim}-100$ km s^{-1}), as well as two upper limits – 10 kpc for the high-latitude part of complex A ($v_{\rm LSR}{\sim}-150$ km s^{-1}), based on the RR Lyrae star AD UMa (van Woerden et al. 1999), and 13 kpc for complex WE ($v_{\rm LSR}{\sim}+110$ km s^{-1}), using the O9.7II star HD 156359 (Sembach et al. 1993). Since then, Wakker et al. (2003) has reported a lower limit of 8 kpc for complex A, while Thom et al. (2006) used the star HE 1048+0231 to set an upper limit of 8.8 kpc to cloud WW 35 ($v_{\rm LSR}{\sim}+100$ km s^{-1}).

In this paper we report on our observations of 25 targets in the direction to two HVCs and two IVCs. These yield distance brackets to all four clouds. We describe the method used to derive the distances of these clouds in Sect. 2. Sect. 3 summarizes our observations, while the manner in which we make our measurements is discussed in Sect. 4. Section 5 presents the results for each of the four clouds, describing the distance determination, notes on each of the stars, a summary of Ca II/H I ratios, a discussion of the implied location in

the Milky Way and a discussion of their ionized hydrogen content. In Sect. 6 we present a short general discussion of our results, while in Sect. 7 we summarize the conclusions.

2. Determing HVC/IVC distances

2.1. Basic method

The distance to an HVC/IVC can be determined by looking for interstellar absorption at the velocity of the cloud in spectra of stars with known distances. A detection sets an upper limit, while a *significant* non-detection sets a lower limit. A significant non-detection means that the ratio of the expected equivalent width to the observed upper limit is sufficiently large (e.g. >10; the exact value depends on the ion that is observed, and on knowledge of the cloud's ionic abundance, see Wakker 2001). The best kind of stars for this purpose are Blue Horizontal Branch (BHB) and RR Lyrae stars (in their hot phase). This is because they are fairly numerous, their distances can be determined relatively well, and they are relatively blue, resulting in few confusing stellar lines. This method is described in detail by Wakker & van Woerden (1997) and Wakker (2001).

There are three steps in the method: (1) locate candidate probe stars, (2) obtain intermediate-resolution spectra and photometry to derive their distances, velocities and abundances, and (3) obtain high spectral resolution (15 $\mathrm{km\,s^{-1}}$ or better) and high signal-to-noise ratio spectra for stars at a range of distances; these stars should be selected to have minimal blending between stellar and interstellar lines. In this paper, we only summarize steps (1) and (2), while we report on the most extensive set of step (3) observations presented in the literature so far. Our extensive program covering steps (1) and (2) will be described in subsequent papers.

2.2. Stellar probes

Until recently, most of the candidate stellar probes were found from three catalogues: the variable star lists of Kukarkin (1969, 1970), the PG survey (Green et al. 1986) and the HK survey (Beers et al. 1996). These list many BHB and RR Lyrae candidates with distances up to about 5 kpc, as well as a few more distant stars (up to ∼10 kpc). The recent data from the Sloan Digital Sky Survey (SDSS) and the 2-Micron All-Sky Survey (2MASS; Cutri et al. 2003) now allow us to make further progress, adding candidate stars at up to 100 kpc distance.

The SDSS project and the creation of the archive are discussed by York et al. (2000). The details of the data products are described by Stoughton et al. (2001) and by Adelman-McCarthy et al. (2005 and references therein). A 2.5-meter telescope (Gunn et al. 2006) is equipped with two dual-beam spectrographs (R$\sim$1800), operating between 3900 Å and 9000 Å, and with a CCD camera (Gunn et al. 1998) with a 5 filter photometric system (Fukugita et al. 1996), calibrated on imaging nights with a 20-inch Photometric Telescope (Hogg et al. 2001, Smith et al. 2002; Ivezic et al. 2004; Tucker et al. 2006). The CCD camera is used to scan the northern sky in the five filters, from which our RR Lyrae or BHB candidate stars are chosen, using color criteria (Sirko et al. 2004; Ivezić et al. 2005). The star positions are determined in the manner described by Pier et al. (2003). These stars have distances ranging from $\sim$5 kpc up to 100 kpc, as estimated from their V magnitudes (V=0.56r+0.44g+0.056; Ivezíc et al. 2000) and assuming an absolute magnitude of M_V=0.7 for RR Lyraes (Layden et al. 1996) and M_V=1.040 + (B−V)*(−4.423+(B−V)*(17.74+(B−V)*(−35.73))) for BHBs (Preston et al. 1991).

The 2MASS survey scanned the sky at 2″ pixels, using automated 1.3m telescopes on Mt. Hopkins and CTIO, taking images at J, H, and K. It includes thousands of BHB candidates with distances up to $\sim$8 kpc, which can be selected from their J−H and J−K colors (Brown et al. 2004).

For some stars the SDSS provides intermediate-resolution ($\sim$2 Å) spectra. To obtain similar spectra for more SDSS stars, as well as for the 2MASS selected stars, we have a large observing project underway at the 3.5-meter telescope at Apache Point Observatory (APO). Between 2003 and 2006 we obtained spectra at APO for some 200 stars.

Using these spectra, we can derive the effective temperature and gravity for each star, following the method outlined by Wilhelm et al. (1999). Combining with photometry these parameters can be used to derive good distance estimates. We will describe these observations (as well as improvements to the original method) in a separate paper (Wilhelm et al. 2007, in preparation). Here we just present an outline.

Our method compares the observed photometry (either SDSS ugr or Johnson UBV), and observed spectroscopy. We compare the Balmer line widths and equivalent width of the Ca II K line with a grid of sythetic colors and spectroscopy parameters that are generated from *Atlas9* model atmospheres. Combining the Balmer line widths with u−g (or U−B) color indices allows the determination of $\log g$ values across the temperature range 6000<$T_{\rm eff}$<12000 K. The determined stellar parameters ($T_{\rm eff}$, $\log g$ and [Fe/H]) are then used to estimate absolute magnitudes M_V by placing the star on the theoretical isochrones of Girardi et al. (2004). This method allows the determination of distances for stars of various metallicities on the zero-age horizontal branch, on the main-sequence, as well as for terminal

HB stars and post-main sequence blue stragglers. We estimate errors in the stellar parameters by changing the input values for observables (i.e. line widths and colors) by $\pm 1\sigma$ one observable at a time. We thus recalculate $T_{\rm eff}$, $\log g$, [Fe/H], M_V, and D many times. The error follows as the rms spread in the set of results for each parameter.

2.3. Implementation

The results of the programs described above yield a sample of stars with known distances in the direction of HVCs. These then need to be observed with high spectral resolution (R>20000), in order to separate the different interstellar absorption components, as well as to maximize the sensitivity to the $\sim$20 km s^{-1} wide HVC/IVC absorptions. In principle, Mg II$\lambda\lambda$2796.352, 2803.531 and C II$\lambda\lambda$1036.337, 1334.532 are the best lines, as they saturate at low H I column densities ($\sim 7\times10^{17}$ cm^{-2}). However, they require sparsely available time on telescopes in space, which are not sensitive enough to observe many 16th to 18th magnitude BHB stars.

In the optical the strongest absorption lines are the Ca II$\lambda\lambda$3934.770, 3969.591 K and H lines. Previous observations of Ca II absorption in HVCs with bright 21-cm emission have yielded six detections, giving Ca II/H I ratios of $17\pm6\times10^{-9}$ for complex A (Schwarz et al. 1995), $22\pm1\times10^{-9}$ for complex C (Wakker et al. 1996), $3.3\pm0.9\times10^{-9}$ for complex M (Bowen et al. 2000), $33\pm4\times10^{-9}$ for the Magellanic Stream (Songaila & York 1981), $66\pm8\times10^{-9}$ for the Leading Arm of the Magellanic Stream (West et al. 1985) and $270\pm120\times10^{-9}$ for complex WB (Robertson et al. 1991). There are also several Ca II detections toward extragalactic supernovae in directions with very faint or no 21-cm (d'Odorico et al. 1985, 1989; Meyer & Roth 1991; Vladilo et al. 1994; Ho & Filippenko 1995, 1996), which yield very high Ca II/H I ratios. Toward IVCs Ca II/H I ratios range from 8×10^{-9} to 55×10^{-9} in the IV Arch, from 12×10^{-9} to 17×10^{-9} in the LLIV Arch, 90×10^{-9} in complex K, 50×10^{-9} in the PP Arch, and 65×10^{-9} in complex gp (Wakker 2001).

Using these detections of high- and intermediate-velocity absorption (as well as HVC/IVC absorption in other ions, such as Fe II) Wakker & Mathis (2000) discovered that for Ca II, Fe II, etc. the [ion]/H I ratio correlates with N(H I). The physical origin of this effect remains unexplained, as discussed by Wakker & Mathis (2000). For Ca II this correlation can be expressed as:

$$R(\mathrm{CaII}) \;=\; N(\mathrm{CaII})/N(\mathrm{HI}) \;=\; -0.78\ (\ \log(\ N(\mathrm{HI}) \;-\; 19.5\ )\ ) \;-\; 7.76.$$

In fact, this relation is a better predictor of the Ca II/H I ratio than the assumption that R(Ca II) is constant in a particular cloud. Therefore, we use this relation to convert the

known H I column densities in HVCs and IVCs in the direction of a candidate target star to predict the Ca II equivalent width. This allows us to construct a sample of stars for each HVC by selecting the ones with the largest predicted equivalent widths in a set of distance intervals (e.g. 1–3 kpc, 3–6 kpc, 6–9 kpc, etc.). We have done this for sixty HVC/IVC fields. In this paper we report on observation of stars in three fields, covering two HVCs and two IVCs.

Previous authors have set distance brackets or limits to HVCs/IVCs using the nominal distances to stars that give upper limits and significant lower limits. However, the errors in the stellar distances have been ignored in the past. In this paper we take them into account. Since the error distribution is centered on the nominal distance, the probability that the upper limit is less than the *nominal* distance to the star is 50%. If the error distribution of the stellar distances were gaussian, the probability that the upper limit is less than $D_{\rm nom}$+0.47$\sigma(D)$ is 68%. Thus, the 68% (i.e. 1σ) confidence interval on the upper distance limit to the HVC is given by $D_{\rm nom}$+0.47$\sigma(D)$. A similar reasoning provides the lower limit of the bracket. At present, we do not calculate the actual error distribution for the distance, so for convenience we assume it is gaussian. For future work we will improve this step.

3. Observations

3.1. Stellar data

For the April-September 2006 semester we were given an allocation of 37 hours on ESO's Very Large Telescope (VLT) to observe 24 stars and one QSO (proposal ID 077.B-0359). For our observations we used the UVES spectrograph installed on the VLT together with a 1″ slit and the blue arm (CD2). This setup provides a wavelength coverage from ∼3730 to 4990 Å, a pixel size of 0.03 Å (∼2.3 km s^{-1}), and a spectral resolution of R∼40,000, corresponding to an FWHM of ∼7.5 km s^{-1}. During our observations the seeing typically was ≤0.″8. The raw data were reduced with the standard UVES pipeline, which includes flat-fielding, bias- and sky-subtraction, and a relative wavelength calibration. To compare with the 21-cm data, the final spectra were then shifted to an LSR velocity scale. For multiple integrations of the same background source, the individual spectra were co-added, weighted by their inverse variances. In the continuum the signal-to-noise ratio (S/N) per resolution element in the UVES data typically ranges from about 40 to 100.

The three HVCs that we selected for our VLT observations have in common that they are above the horizon during the southern winter. They are the "Cohen Stream", "com-

plex GCP" and "cloud g1". Most stars in the Cohen Stream field also lie projected onto another, more nearby IVC. We describe these clouds and the stars projected on them in the next section. Figure 1 shows the locations of these three clouds on a map of the HVC sky. The map also shows the three stars toward which HVC absorption was found previously.

Table 1 presents the stellar data. Coordinates are defined in the names for 2MASS and SDSS stars, given in the notes for the remaining stars. The two "BS" stars are from the HK survey (Beers et al. 1996) and the numbers represent plate number and star id on that plate. Seventeen stars in the VLT sample have classification spectra from our APO observations, one spectrum is from the SDSS (see Col. 2 of the table). We also obtained photometry for most stars, with the source of the data listed in Col. 3 and the resulting magnitudes in Cols. 4, 5 and 6. The extinction (from Schlegel et al. 1998) is given in Col. 7. For five stars we can use SDSS photometry. For twelve stars (eleven from 2MASS, one from the HK survey), we obtained this photometry ourselves. For seven stars we do not have photometry data. Three of these are 2MASS stars, so we used the star's B magnitude from the 2MASS catalogue. For the three named RR Lyrae stars we used the photometry listed in the Kukarkin et al. (1970) catalogue. Finally, Strömgren photometry was obtained by Moehler et al. (1990) for PG 0142+148.

For all stars we give the stellar parameters derived directly from the high-resolution spectra, while for the 17 stars with intermediate-resolution spectroscopy we give additional lines showing the stellar parameters resulting from our APO data, for comparison. The stellar parameters are derived using the photometry, the Balmer lines, Ca II K and H and Ca Iλ4227.918. A full description of this method will be given by Wilhelm et al. (2007, in preparation). Columns 8 to 11 list the resulting effective temperature, gravity, metallicity and stellar type, respectively. Combining the stellar parameters with photometry and isochrones, we can derive the star's distance, given in Col. 13 of the table.

The VLT data were used to derive the stellar velocities listed in Col. 12. This was done by fitting a gaussian to the stellar Ca II, Ca I and Fe I lines, then averaging the fitted central velocities. For some of the stars the stellar velocity varies between exposures (see the notes to the Table). In these cases, we did not use all of the exposures, but only the ones with the least confusing separation between stellar and interstellar lines. The listed velocity is valid for that spectrum.

There are often differences in the temperature, gravity and metallicity derived from the VLT spectrum when compared to those values derived from the APO spectra. When the differences are more than one sigma, they are noted in the following subsection.

3.2. Distance estimation

3.2.1. Non-problematic stars

For eight stars (2MASS J014936.48+143914.6, 2MASS J021409.31+090105.3, 2MASS J195927.29+000822.3, 2MASS J195823.36-002719.0, 2MASS J195912.00-002645.3, 2MASS J213327.04+133026.7, 2MASS J213520.04+133045.0, BS 17578-0016), the determination of the stellar distance based on the VLT and APO spectra is the same to within 15%. For four stars (2MASS J014825.88+132305.3, SDSS J014843.61+130411.5, 2MASS J195922.75+000300.0 and 2MASS J213451.58+134017.5 the determinations differ by 20–40%. Since they are still the same within $\sim 1\sigma$, the results are still compatible, just relatively inaccurate.

In the case of 2MASS J213451.58+134017.5 the metallicity indicated by the Ca II K line is about 1 dex less than that found from spectral regions with many metallic lines (mostly Fe). The star is probably a main-sequence star with solar abundance, so we adopt a nominal $\log g$=4.0 to derive the distance. The lower resolution of the APO data makes that result less reliable, so we are not worried by the $\sim 1\sigma$ difference in the nominal distance.

For one star (2MASS J195925.49−000519.1) the difference between the distance derived from the high- and the intermediate-resolution spectrum is larger than the nominal error (1.5±0.2 kpc vs 2.6±0.4). However, these values are still somewhat consistent, and this is not an important star for our program to determine HVC distances. We therefore did not try to correct his discrepancy.

For two stars (SDSS J015735.65+135254.2, and BS 17578-0015), we have no APO classification spectrum, but we do have photometry, and we are confident that the resulting classifications and distances are good.

Two stars are too hot (i.e. T>12000 K) for our method, but distances are given in the literature. These are PG 0142+148, which was analyzed by Moehler et al. (1990) and PG 2134+125, which is the central star of the planetary nebula NGC 7094. Phillips (2004) summarizes distance determinations for planetaries, and includes NGC 7094.

3.2.2. Problematic stars (non-RR Lyrae)

For two stars the distances derived from the VLT and APO spectra differ substantially.

The VLT spectrum of 2MASS J021651.34+080150.2 shows many stellar lines, which blend in the APO spectrum, making it difficult to determine the gravity. In addition we do not have photometry for this star, so that we cannot directly fit $T_{\rm eff}$ and $\log g$ (see Wilhelm et

al. 2007). We instead use a grid of spectral models with different temperatures and gravities, and find the best match. As a result of these problems, the APO spectrum suggests low gravity, while the VLT spectrum indicates high gravity. This leads to a dichotomy in the classification; we have more confidence in the lower (VLT-based) distance.

The VLT spectrum of 2MASS J195741.61-004009.7 also shows many stellar lines. In fact, the line density is such that it explains why the APO spectrum of this star is noisy, making its analysis difficult. The determination of the star's gravity is so uncertain that the APO data suggest it is a BHB, implying D11.1±3.3 kpc, while the VLT spectrum indicates a main-sequence F star at 0.7±0.6 kpc. We judge that it is more likely to be nearby than to be distant.

3.2.3. RR Lyrae stars

The final five stars are RR Lyrae stars, a classification based on the derived stellar parameters, but also on the fact that we can see the stellar lines shift between different VLT exposures. To estimate a distance for an RR Lyrae star requires a determination of its average magnitude. We usually do not have phase information, so we do not know whether the VLT spectrum or the SDSS photometry was taken during maximum, minimum or somewhere between. Moreover, the magnitudes given by Kukarkin et al. (1970) for V1084 Aql, V1172 Aql, and FW Peg are photographic, not UBV. They are also quantized, in steps of ∼0.25 magnitudes. Therefore, we use the following reasoning to estimate the distances to the five RR Lyrae stars in our sample.

We start by looking at SDSS J015133.91+141105.2. The SDSS photometry of this star gives V=16.81 (using the transformation from $ugriz$ to UBV given by Ivezić et al. 2000). We have six VLT exposures of this star, taken 28 and 16 days apart, with one run of four exposures in four consecutive hours. The star's flux varies between 6.2×10^{-16} erg cm^{-2} s^{-1} Å^{-1} and 20.5×10^{-16} erg cm^{-2} s^{-1} Å^{-1}, giving 13.3×10^{-16} erg cm^{-2} s^{-1} Å^{-1} on average, corresponding to V=16.14. Since the range in flux is about 1.3 magnitude, it is reasonable to conclude that 16.1±0.2 is a good estimate for the average magnitude of this star. Combined with an absolute magnitude for RR Lyraes of M_V=0.7 (Layden et al. 1996) and extinction A_V=0.16 (Schlegel et al. 1998), this implies a distance of 11.2±1.0 kpc.

The flux of SDSS J020033.49+141153.9 varies from 10.7×10^{-16} to 21.6×10^{-16} erg cm^{-2} s^{-1} Å^{-1} between the three spectra of this star. The average flux is about 16×10^{-16} erg cm^{-2} s^{-1} Å^{-1}, or V∼16.0. The temperature that is derived is about 6600 K, which suggests the star is in its cool phase. The SDSS equivalent V magnitude is 15.58. These results are compatible

if the SDSS observation caught it near average while the VLT observation caught it near minimum. Based on this, we set the average magnitude to V=15.6±0.3. With A_V=0.19 this implies D=8.7±1.3 kpc.

For V1084 Aql Kukarkin et al. (1970) gave $<P>$=17.0. Bond (1978) included this star in a sample of RR Lyraes for which he obtained photometry. He finds $<V>$=17.0, with an accuracy of about 0.2 mag. The star's flux varies from 7.4×10^{-16} to 14.5×10^{-16} erg cm^{-2} s^{-1} Å^{-1} in our four VLT exposures. On average this flux corresponds to V=16.35. We derive a temperature of 7000 K, which suggests we observed the star near maximum phase, which is compatible with the relatively high flux and the relatively low number of stellar lines. Using A_V=0.49 (Schlegel et al. 1998) then implies a distance of 14.5±1.3 kpc.

Kukarkin et al. (1970) give an average magnitude for V1172 Aql of 16.5±0.25. We find an average flux in the VLT spectra that corresponds to V=16.36. The temperature that is derived from the three VLT exposures is about 6500 K, suggesting we observed it in a cooler, fainter phase. We thus assume that the Kukarkin et al. (1970) magnitude is slightly low and calculate the distance using $<V>$=16.4±0.3, which for A_V=0.60 gives D=10.5±1.4 kpc.

The star FW Peg has $<V>$=14.0 in Kukarkin et al. (1970). The VLT spectrum gives a flux corresponding to V=14.68, and a temperature of 6500 K. This is compatible if we caught the star near minimum. We thus use $<V>$=14.0±0.5 to calculate its distance. With A_V=0.40 this gives 3.8±0.8 kpc.

4. Measurements

We now summarize the measurements we made on the stars, and then discuss for each cloud in turn our previous knowledge, followed by a more general discussion of our results concerning their distances, Ca II/H I ratios and location in the Milky Way.

4.1. Stellar measurements

Table 2 presents the stellar data that pertain to searching for the interstellar lines. We give the star's Galactic location in Cols. 2 and 3, and repeat the distance from Table 1. Column 5 gives the total VLT exposure times (but see the notes to the table for exposures that were excluded for the final analysis). We also determined the star's continuum flux, as well as the flux and S/N ratio at the velocity of the high-velocity clouds (Cols. 6, 7, 8). This was done by fitting a polynomial to the line-free regions of the continuum. To calculate the flux at the HVC's velocity, the stellar Ca II absorption was considered as "continuum",

since we are interested in the flux and S/N appropriate for measuring the interstellar line against the background of the stellar flux. The order of the fitted polynomial lies between 1 and 4. The signal-to-noise ratio is calculated per 7 $\mathrm{km\,s^{-1}}$ resolution element, i.e. calculated after rebinning the spectrum to three pixels. It is the ratio of the flux to the rms of the fit around the line-free regions of the spectrum used in the fit. This value is compared with the nominal error in the flux to make sure that it is similar.

4.2. H I and Ca II measurements

Table 3 lists the Ca II interstellar measurements. The table contains the following columns.

Columns 1 and 2 repeat the stellar name and distance.

Columns 3 and 4 give the velocity and the logarithm of the H I column density of the HVC, IVC, or low-velocity gas in the sightline. The H I 21-cm emission data were taken from the Leiden-Argentina-Bonn Survey (LAB; Kalberla et al. 2005). This survey provides spectra on a $0\overset{\circ}{.}5\times0\overset{\circ}{.}5$ grid, with a $36'$ beam. We calculated a weighted average of all spectra that lie within $0\overset{\circ}{.}6$ from each star as the best approximation to the H I spectrum toward each star. To determine v(H I) and N(H I) we fitted gaussians to these spectra, using one gaussian component for the high- or intermediate-velocity emission, and between two and four for the low-velocity gas. It should be noted that the intermediate- and high-velocity components usually are not exactly gaussian, so the fit gives only an approximation to N(H I).

The uncertainty in N(H I) is dominated by the fact that the Dwingeloo telescope has a large beam on the sky. Wakker et al. (2001) showed the value of N(H I) measured with a 9 arcmin beam can be up to a factor of 2.5 lower or higher than the value measured with a 35 arcmin beam. Further, when comparing measurements of N(H I) made with a 9 arcmin beam with those made with a 1–2 arcmin beam, the latter are between 75 to 125% of the former. The origin of these differences is clearly small-scale structure in the cloud, including edge effects if the beam is near a cloud's edge. The distribution of the ratio N(H I,real)/N(H I,LAB) has an average of about 1, and an rms of about 0.2. As a result, we assume a 20% error for N(H I) when calculating Ca II/H I ratios. Ideally, we would like to obtain high-resolution (1 arcmin or better) H I 21-cm data toward each of our targets, but we do not have such data at this time. Even then, there is always the possibility of a hole in the distribution of the H I in the direction of the star, and a non-detection would still not imply that the star lies in front of the HVC. However, we use to the apparent hierarchical structure of the H I in HVCs (see Schwarz & Wakker 2004) to argue that it is possible to

account for the uncertainty in N(H I) by using a "safety factor", as described below under the discussion of Col. 13.

Columns 5 and 6 give the predicted K (Col. 5) and H (Col. 6) equivalent widths. These are derived from a predicted Ca II column density, combined with the observed linewidth of the H I emission. The prediction for the column density is derived from the correlation between N(Ca II) and N(H I) discovered by Wakker & Mathis (2000), but with a cloud-dependent correction factor. The correction factor is found by comparing the nominal prediction (given a value of N(H I)) for the Ca II/H I ratio with the actual observed value, and then averaging the resulting quotient between all detections found for each cloud. We will discuss the correction factors in Sect. 4, but note here that the quotient of nominal prediction and actual value tends to be a constant value in a particular cloud, though it varies between clouds.

Columns 7 and 8 list the measured K and H line equivalent width detections or 3-σ limits. For detections the absorption lines were integrated over the range of velocities where the flux lies below the continuum, which is 20–25 km s^{-1} wide for the Cohen Stream, the IVC projected onto the Cohen Stream, and for complex GCP, and about 40 km s^{-1} wide for cloud g1. The equivalent width limits for non-detections were determined by integrating the spectrum over a 20 km s^{-1} velocity range, and setting the upper limit to three times the one sigma error in the equivalent width. The equivalent width error includes the uncertainty associated with the noise, as well as the uncertainty associated with continuum placement.

In Cols. 9 and 10 we give the Ca II column density derived by integrating the apparent optical depth profile (Savage & Sembach 1991):

$$N = \int N_a(v)dv = \frac{m_e c}{\pi e^2} f \lambda \ \ln \frac{C(v)}{F(v)},$$

where $C(v)$ is the continuum and $F(v)$ the observed flux.

The resulting column densities are divided by N(H I), giving the values in Cols. 11 and 12. We note that the error in the Ca II/H I ratio is calculated using the observed error in the Ca II column density combined with an assumed 20% error in N(H I).

Column 13 shows the final result derived from each star: an "U" if the star yields an upper distance limit, an "L" if it gives a lower limit and a blank if the S/N ratio was insufficient to derive a lower limit from a non-detection. The significance of the non-detections is obtained by comparing the expected value (Cols. 5 and 6) with the 3σ upper limits (Cols. 7 and 8). As discussed by Wakker (2001), a safety factor needs to be taken into account for such a comparison, since we do not precisely know the H I column density (see discussion of Col. 4 above) and the Ca II/H I ratio in the cloud may in principle vary due to variations in

calcium depletion and ionization conditions. We assume a factor ∼1.5 for the uncertainty in N(H I) and another factor ∼2 for the uncertainty in the Ca abundance. Only if the ratio EW(expected)/σ(EW) is >9 do we conclude that a non-detection sets a lower limit to the cloud's distance.

4.3. Calculation of masses and mass flow rates

After we determine the distance to a cloud, we can estimate its location in the Milky Way, its mass, and the mass flow rate associated with it. These numbers are summarized in Table 4.

We estimate the mass in the manner described by Wakker & van Woerden (1991). In summary, we find the values of T_B for each point in the cloud that were given by Hulsbosch & Wakker (1988). Converting T_B to a column density (using the linewidth), and then multiplying by the area (in cm^{-2}) represented by one survey grid cell (about one square degree) gives the H I mass in the grid cell. Integrating over the cloud gives the total mass, given an assumed distance, D. This value scales as D^2.

We use the Hulsbosch & Wakker (1988) dataset instead of the newer LAB data from Kalberla et al. (2005), because in the latter we have to select a fixed velocity range, so there can be blending with lower-velocity gas. Also, the cloud edges need to be defined by polygons. The older survey clearly separates any particular HVCs from other gas. An improved list could be constructed from the LAB survey, but this has not yet been done. Where possible we do check the Hulsbosch & Wakker (1988) cloud masses against a rough estimate using the LAB survey, and find that they are similar to about 25%.

To derive the mass flow rate, we need to estimate a vertical velocity for each survey grid cell. Given the observed LSR velocity, we calculate the "deviation velocity" ($v_{\rm DEV}$), the amount by which the cloud's velocity differs from the maximum velocity that can be understood from a simple model of differential galactic rotation (see Wakker 1991). This simple model consists of a disk with radius 26 kpc with thickness 4 kpc inside the solar circle (8.5 kpc) increasing to 12 kpc at 26 kpc. The rotation curve is flat, except in the inner 0.5 kpc where solid-body rotation is assumed. Using the deviation velocity we estimate the cloud's z-velocity (v_z) by assuming that it is purely vertical or by assuming that it is purely radial with respect to the Sun. In the former case, v_z=$v_{\rm DEV}/\sin b$, while in the latter v_z=$v_{\rm DEV}\sin b$. To estimate the mass flow, we take the average of these two possibilities. Dividing the cloud's distance by the estimated vertical velocity yields the time it will take for the cloud to reach the Galactic plane. Finally, the quotient of cloud mass and travel time

gives the mass flow associated with the cloud. The resulting number scales as D.

4.4. Ionized hydrogen

To fully understand the clouds and estimate the mass flows associated with them, we also need to estimate the amount of ionized hydrogen. It turns out that Hα data exists for each of our clouds. There are a number of single pointings for complex GCP and the Cohen Stream, and there are maps from the Wisconsin Hα Mapper (WHAM) northern sky survey (Haffner et al. 2003) for cloud g1 and the Cohen Stream field IVC. We will describe these data when discussing each cloud.

Since we know the cloud distances, we can use the Hα data to estimate the amount of ionized hydrogen in our clouds. There are two ways to do this. In both cases we assume that $N(\mathrm{H}^+)$ is constant, which is justified if the ionization is due to photons from the Galactic disk: hydrogen ionization continues until all Lyman continuum photons have been soaked up. Then, we can first assume that the ionized hydrogen is distributed throughout the cloud, in which case the cloud thickness we use to convert the emission measure to a density is similar to its width on the sky. We can also assume that all the ionized hydrogen sits on the surface of the cloud, and the cloud's density is constant, i.e. we use $n(\mathrm{H}^+)$=n(H I) and calculate the emission length from the emission measure. Both these methods are used to derive the numbers presented in Table 4.

5. Results

5.1. Cohen Stream

5.1.1. Distance

The first cloud we observed is part of the so-called "Cohen Stream", discovered by Cohen (1981) (although he only observed the part of the stream that lies to the east of our stars). This HVC is a rather linear stream of gas that runs from $(l,b)\sim(175°,-30°)$ to $(l,b)\sim(140°,-52°)$, with velocities of $v_{\rm LSR}\sim-110$ km s^{-1}. It lies in a part of the sky where the maximum velocity expected from differential galactic rotation is -15 km s^{-1}. A partial map of the cloud is given in Fig. 2. On its eastern end (l>156°) it overlaps with a bright HVC at $v_{\rm LSR}$=-280 km s^{-1}, also discovered by Cohen (1981), and named WW 507 by Wakker & van Woerden (1991). It is still unclear whether these two HVCs are related or whether they are a chance coincidence. Unfortunately, the footprint of the SDSS does not overlap the

WW 507 cloud, so we do not (yet) know distant stars in its direction. We return to this point in Sect. 5.1.5.

We obtained VLT-UVES spectra for nine stars and one QSO in the direction of the Cohen Stream, shown in Fig. 7. Seven of these objects lie in the direction of the small core at the end of the Stream (cloud WW 516 in Wakker & van Woerden 1991), three lie projected onto its main body (cloud WW 517). As we discuss below, and as can be seen in Fig. 7 and Table 3, we detect high-velocity interstellar Ca II H and K absorption toward the QSO SDSS J014631.99+133506.3 as well as the K line toward the 11.2±1.0 kpc distant RR Lyrae star SDSS J015133.91+141105.2. The most distant star toward which we do not detect the HVC at a significant level is the BHB star 2MASSJ014936.48+143914.63 at 4.6±0.8 kpc. Ca II is also not detected toward SDSS 014843.61+130411.5 (D=5.0±1.2 kpc) and SDSS 020033.50+141154.0 (D=8.7±1.3 kpc). The first of these is not significant, although just barely so, while for the latter the ratio expected/observed equivalent width is only 1. Taking into account the errors on the star's distances, these results imply a distance bracket of 5.0 to 11.7 kpc for the Cohen Stream. If we relax the criterion for a significant non-detection, we could improve the lower limit to 5.6 kpc.

5.1.2. Discussion of stars

1) SDSS J015133.91+141105.2 is the star that sets the upper limit on the distance. The HVC K line is clearly seen in absorption in its spectrum, with an equivalent width of 17±3 mÅ. This low-metallicity ([Fe/H]=−1.73±0.3) AV star shows relatively few stellar lines, and with its velocity of -176 km s^{-1}, the stellar Ca II and Fe Iλ3931.409 lines are shifted well away from the HVC. The expected equivalent width of the H line is 10 mÅ, far below the 34 mÅ detection limit. This detection limit is rather high because the stellar Hϵ line substantially reduces the star's flux at the velocity of the HVC (13.2×10^{-16} erg cm^{-2} s^{-1} Å^{-1} at Ca II K, 3.5×10^{-16} erg cm^{-2} s^{-1} Å^{-1} at Ca II H). Thus, we cannot use the H-line to confirm the K-line detection. However, we have seven exposures of this star, taken on August 10, September 7 (2 exposures) and September 23 (4 exposures one hour apart). These show the stellar velocity varying over time: $v(*)=-194\pm3$ km s^{-1} on August 10, -138 km s^{-1}on September 7, and -178, -193, -193 and -190 km s^{-1} on September 23. From these spectra it is clear that the feature at $v_{\rm LSR}=-104$ km s^{-1} is interstellar, as it stays at the same position, whereas the stellar lines vary. In order to have a clean continuum against which the HVC absorption can be measured, we combined only the first and last exposure, which have the cleanest separation between stellar and interstellar absorption.

2) Toward the QSO SDSS J014631.99+133506.3 the high-velocity cloud's K and H equiv-

alent widths are 17±3 and 11±3 mÅ, respectively. The Ca II/H I ratio implied by the K-line is about half the value found toward the star SDSS J15133.91+141105.2. They differ at the 2σ level, but this can easily be explained by the large uncertainty in the value of N(H I) toward the two targets. On the other hand, the equivalent widths of the K and H lines seen toward the QSO are in the expected ratio of about two, giving confidence in the detections.

3) Using the method described in Sect. 2, we predict K and H equivalent widths of 17 and 8 mÅ toward the 30.4±3.9 kpc distant BHB star SDSS J015735.65+135254.2. In its spectrum we find a possible HVC K absorption of 10±3 mÅ. Since it is just a 3σ feature we do not claim this as a clear detection of the HVC, but the feature is compatible with the expectations.

4) Toward the star 2MASSJ 01449.36.48+143914.6 (D=4.6±0.8 kpc) the ratio of expected Ca II K equivalent width (21 mÅ) to the observed error (2.9 mÅ) is 7.2, which implies that this star sets a lower distance limit to the distance of the HVC.

5) The HVC is also not seen in absorption toward the other six stars with D<10 kpc. Toward most of these stars the H I column density is low, and only the non-detections toward the four nearest stars are significant.

5.1.3. Ca II/H I ratio

The Ca II/H I ratio that we find for the Cohen Stream is on the low end of those found for HVCs: $11.7\pm2.9\times10^{-9}$ toward SDSS J015133.91+141105.2 and $6.8\pm2.0\times10^{-9}$ toward SDSS J014631.99+133506.3. The Ca II/H I ratios predicted by the Wakker & Mathis (2000) correlation are 27×10^{-9} and 17×10^{-9}, respectively. The ratio of observed to expected values thus is 0.42±0.05, i.e. the Cohen Stream appears to be relatively underabundant by a factor of ∼2.4 in gaseous ionized calcium. However, until we have a measurement of the metallicity of the Cohen Stream, it will remain unclear whether this underabundance is due to low metallicity, unusually high calcium ionization or high depletion of calcium onto dust, or even small-scale structure in the H I, which affects our estimate of N(H I).

5.1.4. Location in the Milky Way

Previous assessments of the distance of the Cohen Stream were summarized by Wakker (2001): Kemp et al. (1994) and Tamanaha (1996) observed Mg II, Ca II and Na I in bright stars in the direction of the Cohen Stream, at distances up to 300 pc, but no absorption was found. Based on a morphological study of the high-, intermediate- and low-velocity gas,

Tamanaha (1995) argued that the Cohen Stream is the remnant of a collision between the WW 507 cloud and low-velocity gas, which would place it within about 1 kpc from the disk. Our distance bracket excludes such a simple interaction model, as the cloud is clearly more distant than 9.2 kpc.

It is now clear that this cloud is rather far below the Galactic plane, having z between 3.7 and 8.6 kpc (see Table 4). It is located at similar longitude, but on the opposite side of the plane and further inward than the Galactic warp (which is at galactocentric radii between about 17 and 22 kpc – Burton & te Lintel Hekkert 1986).

5.1.5. Ionized hydrogen

Weiner et al. (2001) reported Hα emission from two directions in the Anti Center region. One of these is at (l,b)= (164°,−46°) and samples the Cohen Stream (Weiner, priv. comm.). The Hα intensity (I(Hα)) is 0.07±0.01 Rayleigh. [One Rayleigh (R) is $10^6/4\pi$ photons cm^{-2} s^{-1} sr^{-1}; the emission measure (EM=$\int n_e^2 L$) is related to this as EM=2.75 $T_4^{0.924}$ I(Hα), where T_4 is the gas temperature in units of 10^4 K].

The H$^+$ column density we derive from the observed Hα emission is on the order of 10^{19} cm^{-2}, independent of most assumptions. The H$^+$ mass is found to be similar to the H I mass, which is a few 10^5 M$_\odot$. If we assume the H$^+$ is located in a layer around the neutral cloud, the implied skin thickness is 10 to 25% of the total cloud thickness.

We noted earlier that Hα emission was also detected from the higher-velocity cloud near the Cohen Stream (Kutyrev & Reynolds 1989; Weiner et al. 2001), with an intensity of ∼0.08 R. This cloud is centered around l=168°, b=−46°, $v_{\rm LSR}$=−280 km s^{-1}. Using the Bland-Hawthorn & Maloney (1999) model of the Galactic ionizing radiation field, the Hα brightness of this cloud would imply a distance on the order of 15 kpc. If such an interpretation for the Hα emission can be maintained, this would suggest that this cloud and the Cohen Stream are close together in space, even though their velocities differ by 170 km s^{-1}.

5.2. High-z Perseus Arm IVC

5.2.1. Distance

In the sightlines to the Cohen Stream an IVC is also visible in the H I spectra, with velocities of ∼−40 to −60 km s^{-1}. This IVC is part of an extended region of intermediate-

velocity gas, a map of which can be found in Wakker (2001; Fig. 18), who named this gas "IV-south". Figure 3 shows the H I with $v_{\rm LSR}$ between -80 and -30 km s^{-1}. In the general vicinity of this IVC differential galactic rotation contributes substantially to the observed radial velocity (up to -15 km s^{-1} at b=$-50°$, up to -45 km s^{-1} at b=$-25°$). Therefore, we present in Fig. 4 the H I column density for deviation velocities between -60 and -30 km s^{-1}, i.e. gas parcels whose velocities are 30 to 60 km s^{-1} more negative from the maximum radial velocity expected from differential galactic rotation. This clearly shows the IVC centered near (l,b)=(145°,$-42°$). The stellar spectra for targets projected onto the IVC can be seen in Fig. 7. The stream running from (l,b)$\sim$(130°,$-60°$) to (l,b)$\sim$(100°,$-47°$) was termed the "Pegasus-Pisces Arch" or PP-Arch by Wakker (2001), and its distance is <2.7 kpc.

Intermediate-velocity absorption is clearly detected toward the QSO and in the spectra of all stars more distant than 2.1 kpc, but not toward PG 0142+148 (D=1.2±0.5kpc), where the ratio EW(expected)/σ(EW) is 12.7. Taking into account the errors on the stellar distances, the implied distance bracket is 1.0 to 2.7 kpc.

5.2.2. Ca II/H I ratio

For this IVC the observed Ca II/H I ratios range from $10\pm3\times10^{-9}$ toward 2MASS J014936.48+143914.6 to 30±9 toward SDSS J015735.65+135254.2. Much of this range might be due to the uncertainty in the H I column densities toward the stars. The ratio of observed to predicted Ca II/H I ratio is on average 0.62±0.11, ranging from 0.41 to 0.75. Thus, like the Cohen Stream, this gas also seems to be deficient in ionized calcium compared to the ratio N(Ca II)/N(H I) for HVCs in general, but we do not have enough information to determine the cause of this.

5.2.3. Location in the Milky Way

The IVC lies below the Perseus Arm, the next spiral arm out from the Local arm. In the Galactic plane, the Perseus spiral arm has velocities of about -50 km s^{-1}. The distance to the Perseus arm is about 2.5±0.5 kpc (see Reynolds et al. 1995 and references therein). Haffner et al. (2005) studied the Hα emission from the high-z extension of the Perseus Arm and find it has a scaleheight of about 1 kpc. Associated gas at b=$-45°$ would be at a distance of 3.6±0.7 kpc and lie 2.5±0.5 kpc below the Galactic plane. A z-height of 1 kpc implies a distance of 1.6 kpc, in which case the cloud would be located in the interarm region. Gas near the upper distance limit of 2.7 kpc would have z=1.9 kpc. So, the IVC we see is likely

associated with the front side of the high-z extension of the Perseus Arm.

For this direction, the LSR velocity predicted from differential galactic rotation is $\sim$−25 km s^{-1}, suggesting that the IVC has a peculiar velocity toward the plane of between 15 and 35 km s^{-1}. The derived distance bracket is not very precise, but it is clearly compatible with the idea that this IVC is associated with the Perseus Arm. This could be confirmed by obtaining spectra with high S/N ratio of additional stars in the 1 to 3 kpc range.

To estimate the cloud's H I mass we integrated the column densities between $l\sim139°$ to 155°, $b\sim-47°$ to −40°. The cloud's total mass is found to be in the range 0.2–1.4×10^4 M$_\odot$. We note that this is of the same order of magnitude as the "Intermediate-Velocity Arch" (IV-Arch), the largest northern IVC (see Kuntz & Danly 1996; Wakker 2001, 2004), which also is moving toward the Galactic plane with a velocity of $\sim$40 km s^{-1}. It is also similar to the mass of the "Low-Latitude Intermediate-Velocity Arch" (LLIV Arch), an IVC that is 0.9–1.8 kpc distant with a mass of 1.5×10^5 M$_\odot$. The latter IVC appears to be in the interarm region. The IVC we detected in absorption may be a cloud similar to the IV and LLIV Arches, but associated with the Perseus Arm, rather than with the Local spiral arm.

5.2.4. Ionized hydrogen

In the WHAM Hα survey (Haffner et al. 2005), there is no detectable Hα emission from the area covered by this cloud, which corresponds to a 3σ upper limit of I(Hα)<0.15 R, or an emission measure <0.07 cm^{-6} pc. The implied H$^+$ column density limit of $\sim$10^{19} cm^{-2} is compatible with the values found for the other clouds. so the non-detection does not imply a lack of ionized hydrogen for this object.

The non-detection does imply that for this cloud the mass of ionized gas is smaller than the neutral hydrogen mass. If the ionized gas is on a skin, this skin is relatively thin, being at most 10% of the cloud's thickness.

5.3. HVC complex GCP or HVC 40−15+100

5.3.1. Distance

The second HVC in our sample lies near l=40°, b=−15° and has $v_{\rm LSR}\sim$90 km s^{-1}. It has been referred to as the "Smith Cloud", after Smith (1963), who discovered it, or as HVC 40−15+100, or as complex GCP (Wakker & van Woerden 1991). Wakker (2001) could only set a lower distance limit of 0.3 kpc, from the non-detection of Ca II absorption toward

some nearby stars.

We observed eight stars projected on complex GCP (see Fig. 5), six of which were found from the 2MASS survey; the other two are RR Lyraes from the Kukarkin (1970) catalogue. The Ca II absorption and H I emission spectra are shown in Fig. 8. We detect the HVC in the spectrum of V1084 Aql, located at 14.5±1.3 kpc, but not toward V1172 Aql at 10.5±1.3 kpc, yielding a distance bracket of 9.8 to 15.1 kpc.

5.3.2. Discussion of stars

1) Figure 8 shows the HVC absorption in the V1084 Aql K-line, which has an equivalent width of 51±3 mÅ. We caught this low-metallicity ([Fe/H]=−1.22±0.25) RR Lyrae star at a temperature of about 7000 K, and the spectrum shows relatively few stellar lines. The Ca II H-line detection is less clear (37±10 mÅ), not only because it is confused by the stellar Hϵ line, but also because the Hϵ lines makes the flux much lower at the HVC's velocity (8.5×10^{-16} erg cm^{-2} s^{-1} Å^{-1} at K, 1.5×10^{-16} erg cm^{-2} s^{-1} Å^{-1} at H).

2) The HVC is absent in the spectrum of V1172 Aql (D=10.5±1.4 kpc), and the ratio expected/error is 15.5 for Ca II K, 7.1 for Ca II H. This star thus yields a lower limit for the HVC's distance. We note that the spectrum of V1172 Aql shows weak (∼25 mÅ) wiggles at the velocity of the HVC in both the K and the H line, but these features don't match up as interstellar Ca II – they are not at exactly the same velocity, and they are not in the ratio 2:1.

3) One other star has a large distance (2MASS J195922.75+000300.0 at 9.0±3.7 kpc), but it has low UV flux as it is a cool star ($T_{\rm eff}$=5750 K), so the non-detection is not significant.

4) The remaining four stars all have distances less than 2 kpc. The non-detections of interstellar Ca II K toward 2MASS J195927.29+000822.3 and 2MASS J195912.00−002645.3 are significant, but for 2MASS J195741.61−004009.7 and 2MASSJ 195925.49−000519.1 this is not the case. Considering the distance bracket we have set, these non-detections are not unexpected since these stars are relatively nearby.

5) Finally, one star in our sample is at about the same distance as V1084 Aql: 2MASS J195823.36−002719.0, at D=13.1±3.2 kpc. The 2MASS catalogue gives a J magnitude of 15.1 for this star, but our photometry (Wilhelm et al. 2007) yields V=16.9. Since we expected the star to be bright (and originally estimated a distance of 5.8 kpc), we only requested a short exposure time (7200 sec). Even less data was actually obtained (2665 sec), so the spectrum has an S/N ratio of only 5 at the location of the interstellar K line. Therefore,

the non-detection is not significant (61 mÅ expected, 3σ upper limit 67 mA).

5.3.3. Ca II/H I ratio

Weighing the K line twice as much as the H line, the average Ca II/H I ratio in complex GCP that we find from the K and H line detected toward V1084 Aql is $6.2\pm1.7\times10^{-9}$. If we estimate EW(K) from the Wakker & Mathis (2000) relation between log R(Ca II) and log N(H I), we predict R(Ca II)$\sim6\times10^{-9}$ for complex GCP. Thus, the Ca II/H I ratio is exactly what is expected.

5.3.4. Location in the Milky Way

We place complex GCP at a distance of 9.8 to 15.1 kpc, which puts it at a galactocentric radius between 6.2 and 9.7 kpc, and 2.5 to 3.9 kpc below the plane. Its $2°\times8°$ size on the sky implies a linear size of about 0.5×1.8 kpc. The H I mass is about 10^6 $M_\odot$.

Bland-Hawthorn et al. (1998) suggested that this HVC is related to the Sagittarius dwarf, at a distance of 26 ± 4 kpc (R=20 kpc, z=−7 kpc). We find that instead of lying on the outskirts of the Milky Way, this HVC is near the solar circle, only halfway to the Sagittarius dwarf. Only a detailed model of the dwarf galaxy's orbit can tell whether the HVC could be related after all.

In the direction of complex GCP differential galactic rotation can explain a velocity of up to +75 km s^{-1}, which occurs at the tangent point (D=7 kpc, at galactocentric radius 5.5 kpc, 2.0 kpc below the plane). At distances of 9.8 and 15.1 kpc, gas in differential rotation has an LSR velocity of +50 and −17 km s^{-1}, respectively. It is therefore clear that complex GCP is below the Galactic plane and moving ahead of the gas in the plane with a velocity of 40 to 105 km s^{-1}. Heroux et al. (in preparation) mapped this HVC using the new Green-Bank Telescope. They are working on a model of its orbit, including drag forces to explain the stretching that is obvious in the sky map (Fig. 5).

5.3.5. Ionized hydrogen

Bland-Hawthorn et al. (1998) based their suggested association with the Sagittarius dwarf on the detected Hα emission from this HVC, with intensities 0.24 R at (l,b)=(40°,−15°) and 0.30 R at (l,b)=(41°,−14°). If we assume that the cloud's thickness is comparable to

the width of its short dimension (0.3–0.5 kpc), these emission measures imply an electron density n_e of 0.04–0.03 cm^{-3}, about 25% of the implied H I density of 0.16–0.10 cm^{-3}. In that case the H^+ mass is similar to the cloud's H I mass. If on the other hand we assume the H^+ occurs around the outside of the cloud, the ionized mass is about a third of the neutral mass, while the skin is about 10% of the thickness of the cloud. In either case it is clear that this cloud must have a substantial ionized component. Now that we know its location, a full Hα map would clearly help understand the Galactic ionizing radiation field.

5.4. Cloud g1

5.4.1. Distance

The last cloud in our sample is an IVC near (l,b)=(67°,−27°), at $v_{\rm LSR}\sim$+70 km s^{-1} (Fig. 6). It is one of a set of faint positive-velocity IVCs in the region l=30° to 70°, b=−45° to −20° that Wakker (2001) termed "complex gp". For the present project we have designated some of the cores in this complex as g1 through g5, with the IVC toward which we observed stars termed "cloud g1". It is, a-priori, unclear whether these IVCs are related to complex GCP, which lies near the IVCs, though at much higher positive velocity.

Many stars projected onto cloud g1 have previously been observed. It was detected in Ca II and Na I absorption toward several stars in M 15 (D=10 kpc; Cohen 1979; Songaila & York 1981; Kennedy et al. 1998; Lehner et al. 1999). Intermediate-velocity absorption at the same velocity as cloud g1 was also seen toward the star HD 203664 (D=4.3±0.4 kpc; Albert et al. 1993; Little et al. 1994; Ryans et al. 1996), which lies three degrees west of the main cloud core (see Fig. 6). Absorption is not detected toward HD 203699 (D=0.8±0.1 kpc; Kennedy et al. 1998), nor toward several A and F stars at distances between 0.2 and 1.4 kpc (Smoker et al. 2001). The non-detections in the latter paper are usually not significant by our criteria, except maybe for their star #7, an A2V star at a distance of 1.4 kpc. Together, these detections and non-detections bracketed the distance of g1 as 0.7 (maybe 1.4) to 4.5 kpc, with the caveat that these stars do not lie near the brighter part of the cloud, but probe the diffuse distribution of gas with similar velocities.

Smoker et al. (2002) made a detailed study of the part the cloud that lies in front of M 15. They combined high angular resolution (1′×2′) H I (Westerbork+Arecibo) data with WHAM Hα profiles and an IRAS map of the region. They found that the H I has structure on scales of 5 arcmin (1.5 D[kpc] pc), and that the gas is warm (∼500 K).

We observed seven stars projected onto the main core of cloud g1, with distances ranging from 1.2 to 8.2 kpc. Since these stars are relatively nearby, the spectra have rela-

tively high S/N ratios. Absorption is seen toward three stars: 2MASS J213327.04+133026.7 (D=8.2±0.9 kpc), FW Peg (D=3.8±0.8 kpc) and BS 17578-0016 (D=3.6±0.5) while significant non-detections are obtained toward the other four stars (ratios of expected EW to upper limit of 25 to 60 for Ca II K). The most distant of these is PG 2134+125 at 2.2±0.8 kpc. Using the 1σ range allowed by the stellar distances, the distance of cloud g1 is then bracketed as 1.8 to 3.8 kpc. This is a range of 2 kpc, tightening the previous 3.8 kpc wide bracket. Unfortunately, the current distance bracket still means that the derived cloud parameters will have an uncertainty of a factor 2 to 4 (depending on how they scale with distance).

5.4.2. Discussion of stars

1) As Fig. 9 shows, the four non-detections toward BS17578-0015, 2MASS J213520.04+133045.0 2MASS J213451.58+134017.5, and PG 2134+125 are very clear. The spectra show no stellar lines near the HVC velocity, and the stellar Ca II K, H and Hϵ lines are not interfering.

2) The detection toward FW Peg is simple and certain: the Ca II K and H absorption lines have equivalent width ratio two, to within the errors. The stellar velocity of -225 km s^{-1} shifts the stellar Ca II K nicely out of the way. Further, we have two spectra of this star (taken 16 days apart) in which the stellar lines clearly shift in velocity, but the lines interpreted as interstellar do not. A few (unidentified) stellar lines can be seen toward more positive velocities than the IVC absorption, but they do not confuse the issue.

3) The detection toward 2MASS J213327.04+133026.7 is not as clean as the one toward FW Peg, but the line is obviously interstellar, since the spectrum shows no stellar lines other than Ca II K, H and Hϵ. However, the Hϵ line is very broad and deep, lowering the flux near the velocity of the interstellar absorption and making the detection of Ca II H more noisy.

4) The most problematic star is BS 17578-0016. Both the H I 21-cm profile and the Ca II absorption lines show two narrow components, separated at the velocity where the H I in g1 usually peaks. This actually gives confidence in the interpretation of the absorption as associated with g1, but it makes the measurements more difficult. In Table 3 we list the absorption as two separate components.

5.4.3. Ca II/H I ratio

As summarized by Wakker (2001), Lehner et al. (1999) detected Ca II in cloud g1 toward 13 stars in M 15. Using values of N(H I) between 42 and 54$\times10^{18}$ cm^{-2} for these stars gives Ca II/H I ratios between 14$\times10^{-9}$ and 79$\times10^{-9}$, averaging to 35$\times10^{-9}$, al-

though individual measurements have large errors. Toward HD 203664 Ryans et al. (1996) derived a Ca II/H I ratio of $450\pm40\times10^{-9}$ (for N(H I)=2.2×10^{18} cm^{-2}). For the three stars toward which we detect cloud g1 we find values of $106\pm22\times10^{-9}$ (FW Peg), 63 ± 1610^{-9} (2MASS J213327.04+133026.7), $109\pm28\times10^{-9}$ (BS 17578-0016, stronger H I component) and $510\pm110\times10^{-9}$ (BS 17578-0016, weaker H I component). Using the Wakker & Mathis (2000) relation, we would predict Ca II/H I ratios of 11×10^{-9} for the stars in M 15, 140×10^{-9} toward HD 203664, and 28×10^{-9}, 35×10^{-9}, 103×10^{-9} and 225×10^{-9} for our detections. The ratio of predicted to observed Ca II/H I ratio thus varies from 1.1 for one of the BS 17578-0016 components, to 3.8 for FW Peg. However, the H I column densities are comparatively uncertain, since the cloud is known to have structure on much smaller scales than the 36′ Dwingeloo beam (Smoker et al. 2002). So, a proper measurement of the Ca II/H I ratios in cloud g1 will require H I observations with much higher resolution toward each of the stellar targets. Nevertheless, it appears that the Ca II/H I ratio is higher than average in cloud g1. Further, the apparently extremely high Ca II/H I ratios for the weak components toward BS 17578-0016 are in line with the values expected from the Wakker & Mathis (2000) relation.

5.4.4. Location in the Milky Way

The distance bracket of 1.8–3.8 kpc for cloud g1 places it at a galactocentric radius of ∼7.9 kpc and z=−0.8 to −1.7 kpc, moving with v=55 km s^{-1} relative to co-rotating Galactic gas around it. The ranges in the implied galactocentric radius and peculiar velocity are small because g1 lies near the tangent point. Its height below the plane is typical for an IVC. However, unlike the large Intermediate-Velocity Arch in the northern sky, this gas is moving away from the plane with an estimated velocity of about 25 km s^{-1}.

The area of the core of the cloud is only about $2^\circ\times2^\circ$, which translates to a size of $(60\text{–}130)^2$ pc. The H I mass is only about 1000–4000 M$_\odot$. The neutral part of this cloud is thus clearly fairly small.

5.4.5. Ionized hydrogen

Smoker et al. (2002) reported Hα emission from cloud g1 toward three directions that lie projected onto the areas with the brightest H I emission. These detections were taken from the WHAM northern sky survey (Haffner et al. 2003). The Hα intensity does not vary much (the detections are 1.30±0.04 R, 0.95±0.04 R and 0.91±0.03 R), whereas the H I column

densities have a range of a factor 3 for these directions. This result supports the contention that for many HVCs/IVCs $I(\mathrm{H}\alpha)$ will be relatively constant across the face of the cloud, and not correlated with N(H I). With our distance bracket for this cloud, the bright Hα intensities imply either a relatively large H^+ volume density ($\sim$0.17 cm^{-3}) or a large ionized pathlength (several hundred pc). With either of our assumptions, $M(\mathrm{H}^+)$ is much larger than M(H I), by at factor 5 to 10. It is clear that what we call cloud g1 is a small neutral condensation in a much larger region of ionized gas.

5.5. Low-velocity gas

Low-velocity Ca II absorption is detected toward all stars, although in a few cases stellar lines make it impossible to measure the equivalent widths. It is likely that the low-velocity absorption is a mixture of several nearby clouds in the line of sight, but we have no way of separating these.

The Ca II/H I ratios measured for the low-velocity gas are similar for the different fields, averaging to $4.4\pm1.6\times10^{-9}$ for stars projected on the Cohen Stream, $5.3\pm1.9\times10^{-9}$ for the complex GCP stars and $5.7\pm2.0\times10^{-9}$ for stars in the cloud g1 field. Applying the Wakker & Mathis (2000) relation, these values are only a factor 2–4 higher than expected. This is remarkable, since that relation was determined using HVC and IVC detections only, and in principle it might not be applicable to low-velocity absorption components since these are probably a mixture of several clouds with different column densities. Also, the column densities of the low-velocity gas are a factor 10 to a 100 larger than the column densities in the HVCs.

In the direction to complex GCP there is an absorption component at $v_{\mathrm{LSR}}\sim30$ km s^{-1} that is detected in every sightline. This component is well separated in the Ca II absorption, but not in the H I profile. To estimate N(H I) we therefore integrated the H I over the same velocity range as the Ca II absorption. The measured Ca II/H I ratio is rather uncertain because the associated H I column density is very difficult to measure. Using a flat rotation curve this gas would have a kinematical distance of 2.0 kpc (R=7.1 kpc, z=−0.5 kpc). This is consistent with the detection toward the star at 1.8±0.3 kpc, but the detections toward the star that are 0.7±0.6 kpc and 1.1±0.5 kpc distant suggest that the gas is much nearer than indicated by the simple kinematical model. At a distance of 0.7 kpc, the expected radial velocity is only $\sim$8 km s^{-1}, so this gas deviates by about 20 km s^{-1} from its expected velocity.

6. Discussion

We now present a short discussion summarizing the implications of our results as they pertain to the mass inflow rate of external gas, to the study of the escape of ionizing radiation from the Milky Way and to the understanding of tidal streams around the Milky Way. We do not give a full discussion of these items – that will be saved for a future paper, after we have determined more HVC and IVC distances.

One of the more important processes that HVCs trace is the infall of low-metallicity materal onto the Milky Way. Wakker et al. (1999) found that HVC complex C (which has a metallicity 0.15 times solar – Wakker et al. 1999; Richter et al. 2001; Tripp et al. 2003; Sembach et al. 2004) contributes a mass inflow rate of about 0.1–0.2 $M_\odot\,yr^{-1}$, assuming a distance of 10 kpc. A similar calculation for HVC complex A shows that it contributes about 0.05 $M_\odot\,yr^{-1}$. Although we do not know the metallicity of the Cohen Stream, its location and velocity leads us to predict that it is a low-metallicity newcomer to the Milky Way. As Table 4 shows, it contributes about 0.01 $M_\odot\,yr^{-1}$.

There are a number of other HVCs that may represent low-metallicity infalling gas. However, we do not have direct data to prove this. These are the HVCs in complexes H, ACHV, ACVHV, GN, P (see Wakker & van Woerden 1991 for the definition). If all of these objects were at a distance of 10 kpc, they would represent an inflow rate of 0.4 $M_\odot\,yr^{-1}$. The Cohen Stream is one of the larger, but not one of the brighter HVCs in the ACHV complex. If all clouds in this complex are 10 kpc distant, the complex as a whole corresponds to a mass flow rate of 0.1 $M_\odot\,yr^{-1}$.

Putman et al. (2004) proposed that most, if not all, of the HVCs in the Anti Center region are in the orbit of the Sagittarius dwarf, and they suggested that this gas was stripped from that galaxy 200 to 300 Myr ago as it interacted with the gas at the far outskirts of the Galaxy. This would imply a distance on the order of 40 kpc for the Anti Center HVCs. We cannot directly exclude that the higher velocity HVC in the region ($v_{\rm LSR}\sim-280$ km s^{-1}) is this distant, but clearly the Cohen Stream is much closer. Moreover, the intensity of the Hα emission from the -280 km s^{-1} cloud is similar to that of the Cohen Stream, which argues that their distances are similar.

We find that the IVC near $(l,b)=(140^\circ,-40^\circ)$ could well be a cloud associated with the Perseus Arm. We do not have an accurate distance, but even so we find that its properties are comparable to those of the two large northern IVCs, the IV-Arch and the LLIV-Arch. Both of these have near-solar metallicity, a mass on the order of 10^5 $M_\odot$, and each represent an inflow of about 5×10^{-3} $M_\odot\,yr^{-1}$(Wakker 2004). Thus, if we were living in the Perseus Arm, this IVC would show up as a fairly large solar-metallicity infalling cloud near the

Galactic south pole.

The g1 cloud has properties just like what is expected for gas taking part in the outflow phase of a Galactic Fountain (see Houck & Bregman 1991). As the hot gas flows out it starts condensing a few kpc up, before it reaches its maximum height (cloud g1 is at $z\sim1$ kpc, moving out with 25 km s^{-1}). The process of ejecting the gas destroys much of the dust, leading to relatively high gaseous abundances (cloud g1 has a larger than average Ca II/H I ratio). But most of the gas is still ionized ($M(\mathrm{H}^+)\sim5$–10 M(H I) for cloud g1). The only thing we still have not measured directly is the metallicity of cloud g1, which will require spectra in the 1000–1300 Å spectra range for UV-bright stars projected onto it. We expect the metallicity to be solar.

Finally, we note that some of the conclusions above can be confirmed by measuring the cloud metallicities. This can be done by determining the abundance of O I, S II and other ions in spectra of UV-bright targets located behind our clouds. A check of the FUSE and HST archives shows that no useful data exists at present. Targets behind the clouds have been observed, but their spectra have too low resolution, there are too many stellar lines, or they are too faint to provide enough background flux.

7. Conclusions

We report on VLT observations of 24 stars and one QSO projected on four high-velocity clouds (HVC). Using these data we derive distances to these objects. We combine H I and Hα data to estimate the total cloud (neutral and ionized) gas masses.

(1) We derive a distance bracket of 5.0 to 11.7 kpc for Cohen Stream, a cloud that is the most-negative-latitude large cloud in the Anti-Center complex of HVCs. This places the cloud between 3.7 and 8.6 kpc below the Galactic plane. The stream runs from $(l,b)\sim(175°,-30°)$ to $(l,b)\sim(140°,-52°)$, and has velocities of $v_{\rm LSR}\sim-110$ km s^{-1}. Ca II K and H absorption is detected toward the QSO SDSS J014631.99+133506.3 with equivalent widths of 17±3 and 11±3 mÅ, respectively. We also find a 17±3 mÅ Ca II K absorption in the spectrum of the 11.2±1.0 kpc distant RR Lyrae star SDSS J015133.91+141105.2. The lower limit is derived from the significant non-detection of high-velocity Ca II toward the BHB star 2MASS J014936.48+143914.6 (21 mÅ line expected, 3σ upper limit 9 mÅ).

(2) The distance bracket for the Cohen Stream implies a total neutral hydrogen mass of 2.5 to 3.9×10^5 M$_\odot$ for the cloud, and an associated mass inflow rate on the order of 0.004 M$_\odot$ yr^{-1}. Hα emission from the Cohen Stream has been detected at one position and its intensity suggests an amount of ionized gas that is comparable to the amount of neutral

gas. The complex of HVCs that the Cohen Stream is a part of would represent a total inflow of 0.1 $M_\odot\,yr^{-1}$ if all clouds in the complex are at similar distances. A direct measurement of the metallicity of this complex is still lacking, so the interpretation of the complex as infalling low-metallicity gas is not confirmed.

(3) We find a rough distance bracket of 1.0 to 2.7 kpc for intermediate-velocity gas in the direction of the Cohen Stream. This suggests that this gas is part of a high-z extension of the Perseus Arm, similar to the more well-studied northern intermediate-velocity clouds. Like these clouds the IVC may be part of a Galactic Fountain flow, but it is associated with the Perseus Arm rather than with the Local Arm.

(4) We determine the distance to HVC complex GCP as 9.8 to 15.1 kpc, based on the detection of Ca II K absorption (51±3 mÅ) in the spectrum of the RR Lyrae star V1084 Aql (D=14.5±1.3 kpc), and the significant non-detection (3σ limit 11 mÅ, expected 59 mÅ) toward the RR Lyrae V1172 Aql (D=10.5±1.4 kpc).

(5) The distance bracket for complex GCP implies the cloud is at a galactocentric radius of 6.2 to 9.7 kpc, lies 2.5 to 3.9 kpc below the plane and has a neutral gas mass of $\sim 10^6$ $M_\odot$. Hα emission is detected from two positions in the cloud and implies an ionized component that is 40 to 120% as large as the neutral component. At its location the cloud is moving with a velocity of 35–75 $km\,s^{-1}$ relative to gas taking part in differential galactic rotation, and it is moving away from the Galactic plane at about 10–20 $km\,s^{-1}$.

(6) For the IVC cloud g1 we derive a distance bracket of 1.8 to 3.8 kpc, detecting the associated absorption in the spectra of three stars 2MASS J213327.04+133026.7 (D=8.2±0.9 kpc), FW Peg (D=3.6±0.8 kpc) and BS 17578-0016 (D=3.6±0.5), but not in four nearer stars. This places the IVC 0.8 to 1.7 kpc below the Galactic disk, and implies that it has a peculiar velocity of about 55 $km\,s^{-1}$. It is a small cloud, with a mass of no more than 10^4 $M_\odot$, and an area of $(60\text{–}130)^2$ pc^2. It is moving away from the Galactic plane with a velocity of about 20 $km\,s^{-1}$. The relatively bright Hα emission coming from this cloud (Smoker et al. 2002) implies that there is a factor 5 to 10 more ionized gas than neutral gas. The most likely interpretation for this object appears to be that it is condensing in an upward Fountain flow.

(7) The Ca II/H I ratios that we derive are all in line with the relation between R(Ca II) and N(H I) that was found by Wakker & Mathis (2000), except that each cloud appears to have a different scaling factor. In particular, the Cohen Stream detections are a factor 0.44±0.5 below the average relation, for the Perseus Arm gas the scaling factor is 0.62±0.11, the complex GCP detection is on the average, while the cloud g1 detections fall a factor 2.2±1.0 above the average.

(8) We have set new distance brackets to four HVCs/IVCs, which trace at least two of the different origins of HVCs: inflow of new material (the Cohen Stream), the Galactic Fountain (cloud g1 and the Perseus Arm IVC). The origin of the fourth cloud (complex GCP) is less clear, but with our distance estimate detailed modeling is now possible. In the future we hope to determine more distances to HVCs/IVCs, and we should eventually be able to measure the inflow rate of accreting material as well as the rate of circulation of gas between disk and halo.

B.P.W., D.G.Y, R.W. and T.C.B. acknowledge support from grant AST-06-07154 awarded by the US National Science Foundation. T.C.B. also acknowledges NSF grant PHY-02-16783; Physics Frontier Center/Joint Institute for Nuclear Astrophysics (JINA).

We thank Ben McCall for help in observing logistics support, the staff of Apache Point Observatory for excellent observing support and Chris Thom for discussions.

Funding for the SDSS and SDSS-II has been provided by the Alfred P. Sloan Foundation, the Participating Institutions, the National Science Foundation, the U.S. Department of Energy, the National Aeronautics and Space Administration, the Japanese Monbukagakusho, the Max Planck Society, and the Higher Education Funding Council for England. The SDSS Web Site is http://www.sdss.org/.

The SDSS is managed by the Astrophysical Research Consortium for the Participating Institutions. The Participating Institutions are the American Museum of Natural History, Astrophysical Institute Potsdam, University of Basel, University of Cambridge, Case Western Reserve University, University of Chicago, Drexel University, Fermilab, the Institute for Advanced Study, the Japan Participation Group, Johns Hopkins University, the Joint Institute for Nuclear Astrophysics, the Kavli Institute for Particle Astrophysics and Cosmology, the Korean Scientist Group, the Chinese Academy of Sciences (LAMOST), Los Alamos National Laboratory, the Max-Planck-Institute for Astronomy (MPIA), the Max-Planck-Institute for Astrophysics (MPA), New Mexico State University, Ohio State University, University of Pittsburgh, University of Portsmouth, Princeton University, the United States Naval Observatory, and the University of Washington.

REFERENCES

Adelman-McCarthy J., et al. 2007, ApJS, in press (Data Release Five)

Albert C.E., Blades J.C., Morton D.C., Lockman F.J., Proulx M., Ferrarese L., 1993, ApJS 88, 81

Beers T.C., Wilhelm R., Doinidis S.P., Mattson C.J., 1996, ApJS 103, 433

Bland-Hawthorn J., Veilleux S., Cecil G.N., Putman M.E., Gibson B.K., Maloney P.R., 1998, MNRAS 299, 611

Bland-Hawthorn J., Maloney P.R., 1999, ApJ 510, L33

Bond H.E., 1978, PASP, 90, 526

Bowen D.V., Roth K.C., Meyer D.M., Blades J.C., 2000, ApJ 536, 225

Brown W.R., Geller M.J., Kenyon S.J., Beers T.C., Kurtz M.J., Roll J.B., 2004, AJ 127, 1555

Burton W.B., te Lintel Hekkert P., 1986, A&AS 65, 427

Chiappini C., Matteucci F., Romano D., 2001, ApJ, 554, 1044

Cohen J.G., 1979, ApJ, 231, 751

Cohen R.J., 1981, MNRAS 196, 853

Cutri R.M., et al. 2003, 2MASS All Sky Catalog of Point Sources (VizieR Online Data Catalog 2246)

d'Odorico S., Pettini M., Ponz D., 1985, ApJ 299, 852

d'Odorico S., di Serego Alighieri S., Pettini M., Magain P., Nissen P.E., Panagia N., 1989, A&Ap 215, 21

Fukugita M., Ichikawa T., Gunn J.E., Doi M., Shimasaku K., Schneider D.P., 1996, AJ, 111, 1748

Gibson B.K., Giroux M.L., Penton S.V., Putman M.E., Stocke J.T., Shull J.M., 2000, AJ 120, 1830

Girardi L, Grebel E.K., Odenkirchen M., Chiosi C., 2004 A&A, 422, 205

Green R.F., Schmidt M., Liebert J, 1986, ApJS 61, 306

Gunn J.E., et al. 1998, AJ, 116, 3040

Gunn J.E., et al. 2006, AJ, 131, 2332

Haffner L.M., Reynolds R.J., Tufte S.L., 1999, ApJ, 523, 223

Haffner L.M., Reynolds R.J., Tufte S.L., Madsen G.H., Jaehnig K.P., Percival J.W., 2003, ApJ, 149, 405

Hartmann D., Burton W.B., 1997, "Atlas of Galactic neutral hydrogen", Cambridge University Press

Ho L.C., Filippenko A.V., 1995, ApJ 444, 165

Ho L.C., Filippenko A.V., 1996, ApJ 463, 818

Hogg D.W., Finkbeiner D.P., Schlegel D.J., Gunn J.E., 2001, AJ, 122, 2129

Houck J.C., Bregman J.N., 1990, ApJ, 352, 506

Hulsbosch A.N.M., Wakker B.P., 1988, A&AS 75, 191

Ivezić Ẑ., et al., 2000, AJ, 120, 963

Ivezić Ẑ., et al., 2004, AN, 326, 583

Ivezić Ẑ., Vivas A.K., Lupton R.H., Zinn R., 2005, AJ 129, 1096

Kalberla P.W.W., Burton W.B., Hartmann D., Arnal E.M., Bajaja E., Morras R., Pöppel W.G.L., 2005, A&A, 440, 775

Kemp S.N., Bates B., Dufton P.L., Keenan F.P., Montgomery A.S., 1994, MNRAS 270, 597

Kennedy D.C., Bates B., Keenan F.P., Kemp S.N., Ryans R.S.I., Davies R.D., Sembach K.R., 1998, MNRAS 297, 849

Kukarkin B.V. et al. 1969, 1970, General Catalogue of Variable Stars, Third Edition, Volumes I and II, Moscow: Sternberg Institute

Kuntz K.D., Danly L., 1996, ApJ 457, 703

Kutyrev A.S., Reynolds R.J., 1989, ApJ, 344, L9

Layden A.C., Hanson R.D., Hawley S.L., Klemola A.R., Hanley C.J., 1996 AJ 112, 2110

Lehner N., Rolleston W.R.J., Ryans R.S.I., Keenan F.P., Bates B., Pollacco D.L., Sembach K.R., 1999, A&AS 134, 257

Little J.E., Dufton P.L., Keenan F.P., Conlon E.S., 1994, ApJ 427, 267

Lu L., Savage B.D., Sembach K.R., Wakker B.P., Sargent W.W.L., Oosterloo T.A., 1998, AJ, 115, 162

Meyer D.M., Roth K.C., 1991, ApJ 383, L41

Maloney P., 1993, ApJ, 414, 41

Moehler S., Heber U., de Boer K.S, 1990, A&A, 239, 265

Morras R., Bajaja E., Arnal E.M., Pöppel W.G.L., 2000, A&AS, 142, 25

Pier J.R., Munn J.A., Hindsley R.B., Hennessy G.S., Kent S.M., Lupton R.H., Ivezic Ẑ., 2003, AJ, 125, 1559

Phillips J.P., 2004, MNRAS, 353, 589

Prata S., Wallerstein G., 1967, PASP 79, 202

Preston G.W., Schectman S.A., Beers T.C., 1991, ApJS 76, 1001

Putman M.E., Thom C., Gibson B.K., Staveley-Smith L., 2004, ApJ, 603, L77

Reynolds R.J., Tufte S.L., Kung D.T., McCullough P.R., Heiles C., 1995, ApJ, 448, 715

Richter P., 2006, Reviews in Modern Astronomy, 19, 31

Richter P., Savage B.D., Wakker B.P., Sembach K.R., Kalberla P.M.W., 2001, ApJ, 549, 281

Richter P, Sembach K.R., Wakker B.P., Savage B.D., Tripp T.M., Murphy E.M., Kalberla P.M.W., Jenkins E.B., 2001, ApJ 559, 318

Robertson J.G., Schwarz U.J., van Woerden H., Murray J.D., Morton D.C., Hulsbosch A.N.M., 1991, MNRAS 248, 508

Ryans R.S.I., Sembach K.R., Keenan F.P., 1996, A&A 314, 609

Savage B.D., Sembach K.R., 1991, ApJS 379, 245

Schlegel D.J., Finkbeiner D.P., Davis M., 1998, ApJ 500, 525

Schwarz U.J., Wakker B.P., 2004, in "High velocity clouds", eds. H. van Woerden, B.P. Wakker, U.J. Schwarz, K.S. de Boer, Kluwer Acad. Press, p145

Schwarz U.J., Wakker B.P., van Woerden H., 1995, A&A, 302, 364

Sembach K.R., Savage B.D., Massa D., 1991, ApJ 372, 81

Sembach K.R., Wakker B.P., Tripp T.M., Richter P., Kruk J.W., Blair W.P., Moos H.W., Savage B.D., Shull J.M., York D.G., Sonneborn G., Hébrard G., Ferlet R., Vidal-Madjar A., Friedman S., Jenkins E.B., 2004, ApJS, 150, 387

Sirko E., Goodman J., Knapp G.R., Brinkmann J., Ivezić Ẑ., Knerr E.J., Schleel D., Schneider D.P., York D.G., 2004, AJ 127, 899

Smith G.P., 1963, BAN 17, 203

Smith J.A., et al., 2002, AJ, 123, 2121

Smoker J.V., Lehner N., Keenan F.P., Totten E.J., Murphy E., Sembach K.R., Davies R.D., Bates B., 2001, MNRAS, 322, 13

Smoker J.V., Haffner L.M., Keenan F.P., Davies R.D., Pollacco D., 2002, MNRAS, 337, 385

Songaila A., York D.G., 1981, ApJ 242 976

Stoughton C., et al. 2002, AJ, 123, 485

Tamanaha C.M., 1995, ApJ 450, 638

Tamanaha C.M., 1996, ApJS 104, 81

Thom C., Putman M.E., Gibson B.K., Christlieb N., Flynn C., Beers T.C., Wilhelm R., Lee Y.S., 2006, ApJ 638, L97

Tripp T.M., Wakker B.P., Jenkins E.B., Bowers C.W., Danks A.C., Green R.F., et al., 2003, AJ 125, 3122

Tucker D., et al., 2006, AN, 327, 821

Tufte S.L., Reynolds R.J., Haffner L.M., 1998, ApJ, 504, 773

van Woerden H., Schwarz U.J., Peletier R.F., Wakker B.P., Kalberla P.M.W., 1999, Nature 400, 138

van Woerden H., Wakker B.P., 2004, in "High velocity clouds", eds. H. van Woerden, B.P. Wakker, U.J. Schwarz, K.S. de Boer, Kluwer Acad. Press, p195,

Vladilo G., Centurión M., de Boer K.S., King D.L., Lipman K., Stegert J.S.W., Unger S.W., Walton N.A., 1994, A&Ap 291, 425

Wakker B.P., 1991, A&A 250, 499

Wakker B.P., van Woerden H., 1991, A&A 25, 509

Wakker B.P., van Woerden H., Schwarz U.J., Peletier R.F., Douglas N.G., 1996, A&A 306, L25

Wakker B.P., van Woerden H., 1997, ARA&A 35, 217

Wakker B.P, Howk J.C., Savage B.D., van Woerden H., Tufte S.L., Schwarz U.J., Benjamin R., Reynolds R.J., Peletier R.F., Kalberla P.M.W., 1999, Nature 402, 388

Wakker B.P., Mathis J.S., 2000, ApJL, 544, L107

Wakker B.P., 2001, ApJS 136, 463

Wakker B.P., Kalberla P.M.W., van Woerden H., de Boer K.S., Putman M.E., 2001, ApJS, 136 537

Wakker B.P., et al. 2003, ApJS, 146, 1

Wakker B.P., 2004, in "High velocity clouds", eds. H. van Woerden, B.P. Wakker, U.J. Schwarz, K.S. de Boer, Kluwer Acad. Press, p26,

Weiner B.J., Vogel S.N., Williams T.B., 2001, in "Gas & Galaxy Evolution", ASP Conf. Series 240, eds. J.E. Hibbard, M.P. Rupen, J.H. van Gorkom, 515

West K.A., Pettini M., Penton M., Blades J.C., Morton D.C., 1985, MNRAS 215, 481

Wilhelm R., Beers T.C., Gray R.O., 1999, AJ 117, 2308

York D.G., et al. 2000, AJ 120, 1579

This preprint was prepared with the AAS LaTeX macros v5.2.

Table 1. Stellar data

object	Tel.[1]	phot[2]	y/V/r[3]	B/g[3]	U/u[3]	E_{B-V}	T_{eff}[4] [K]	$log\ g$[5] [cm s^{-2}]	$logZ$[6] [/$Z_\odot$]	type[7]	$v(*)$[8] [km s^{-1}]	D[9] [kpc]
(1)	(2)	(3)	(4)	(5)	(6)	(7)	(8)	(9)	(10)	(11)	(12)	(13)
PG0142+148[11]	VLT	Str	13.73			0.048	26200	5.10		sdB	−74±2	1.2±0.5
	APO						26200	5.10		sdB	−67	1.2±0.5
2MASSJ014825.88+132305.3	VLT	UBV	13.89	14.06	14.01	0.071	7927±140	4.08±0.78	−1.99±0.12	AV	−167±2	2.1±1.3
	APO						8120±141	4.47±0.63	−1.70±0.12	AV	−155	1.2±0.7
2MASSJ021651.34+080150.2	VLT	2MS	16.80			0.102	6250±250	4.50±0.50	−1.00±0.25	FV	213±1	2.2±1.0
	APO						6250±250	2.75±0.50	−1.25±0.25	FHB	209	21.0±8.6
2MASSJ021409.31+090105.3	VLT	UBV	13.55	13.79	13.95	0.092	7744±46	3.47±0.17	−1.39±0.16	AV	−37±1	3.3±0.8
	APO						7646±76	3.25±0.12	−1.71±0.09	FHB	−2	3.1±0.2
	APO						7749±115	3.53±0.16	−1.14±0.14	AV	−25	3.3±0.6
2MASSJ014936.48+143914.6	VLT	UBV	14.05	14.21	14.27	0.044	8113±106	3.42±0.27	−0.03±0.06	AV	−66±7	4.6±0.8
	APO						7901±233	3.34±0.37	−0.81±0.28	FHB/AV	−30	4.0±1.0
SDSSJ014843.61+130411.5	VLT	SDSS	14.20	14.59	15.84	0.084	5880±112	3.00±0.25	−0.66±0.11	FV	−57±2	5.0±1.2
	APO	UBVS	14.43	15.02	15.07		5774±100	2.75±1.07	−0.89±0.32	FHB	−97	6.3±2.5
SDSSJ020033.50+141154.0	VLT	SDSS	15.48	15.58	16.89	0.059	6644±22	2.00±0.00	−1.32±0.18	RR	−29±3[10]	8.7±1.3
	SDSS	UBVS	15.58	15.87	15.97		6911±21	2.15±0.09	−1.73±0.21	RR	8	
SDSSJ015133.91+141105.2	VLT	SDSS	16.64	16.89	17.94	0.049	6823±312	3.87±0.37	−1.90±0.22	RR	−190±2[10]	11.2±1.0
	APO	UBVS	16.81	17.25	17.15		6530±24	3.12±0.09	−1.73±0.30	AV	−176	
SDSSJ015735.65+135254.2	VLT	SDSS	17.92	17.80	19.01	0.061	8109±156	3.10±0.13	−2.98±0.15	FHB	1±2	30.4±3.9
		UBVS	17.92	17.99	18.01							
SDSSJ014631.99+133506.3	VLT	SDSS	17.23	17.14	17.35	0.057				QSO	0.69[12]	
		UBVS	17.26	17.32	16.60							
2MASSJ195741.61−004009.7	VLT	2MS	16.56	16.90		0.240	6250±250	4.50±0.50	−1.00±0.25	FV	73±2	0.7±0.6
	APO						6250±250	3.25±0.25	−1.25±0.25	FHB	−−[13]	11.1±3.3
2MASSJ195927.29+000822.3	VLT	UBV	14.88	15.28	15.39	0.214	7755±115	4.52±0.25	−1.01±0.09	AV	−1±3	1.1±0.5
	APO						7463±257	4.41±0.35	−0.84±0.26	AV	−35	1.1±0.5
2MASSJ195925.49−000519.1	VLT	UBV	14.24	14.70	14.93	0.215	7660±45	4.18±0.09	−0.14±0.07	AV	34±2	1.5±0.2

Table 1—Continued

object	Tel.[1]	phot[2]	y/V/r[3]	B/g[3]	U/u[3]	E_{B-V}	$T_{\rm eff}$[4] [K]	$log\ g$[5] [cm s^{-2}]	$logZ$[6] [/$Z_\odot$]	type[7]	$v(*)$[8] [km s^{-1}]	D[9] [kpc]
(1)	(2)	(3)	(4)	(5)	(6)	(7)	(8)	(9)	(10)	(11)	(12)	(13)
	APO						7233±124	3.67±0.22	−0.09±0.08	AV	−61	2.6±0.4
2MASSJ195912.00−002645.3	VLT	UBV	13.96	14.42	14.52	0.156	7124±92	3.73±0.04	−0.95±0.06	AV	24±4	1.8±0.3
	APO						7089±88	4.03±0.22	−0.02±0.06	AV	27	1.7±0.4
2MASSJ195922.75+000300.0	VLT	UBV	17.40	18.18	18.33	0.213	5762±81	3.00±0.50	0.00±0.11	FHB	21±2	9.0±3.7
	APO						5750±250	3.00±0.50	−0.75±0.25	FHB/AV	16	11.9±3.9
V1172Aql[14]	VLT	Kuk	16.5			0.182	6500±250	2.50±0.50	−0.85±0.25	RR	−122±1[10]	10.5±1.4
2MASSJ195823.36−002719.0	VLT	UBV	16.85	17.57	17.78	0.203	5911±91	2.50±0.50	−0.35±0.13	FHB	40±2	13.1±3.2
	APO						6164±42	2.39±0.31	−1.01±0.13	FHB	26	11.0±3.0
V1084Aql[15]	VLT	Kuk	17.0			0.148	7000±250	2.50±0.50	−1.22±0.25	RR	−32±2	14.5±1.3
BS17578−0015[16]	VLT	GSC	10.19	10.45		0.110	7125±250	2.50±0.25	−0.50±0.25	FHB	−9±5	1.2±0.3
2MASSJ213520.04+133045.0	VLT	UBV	13.22	13.44	13.74	0.131	7733±58	4.00±0.17	−0.72±0.15	Am	26±6	1.3±0.2
	APO						7794±180	4.00±0.30	−1.55±0.08	Am	−5[10]	1.5±0.5
2MASSJ213451.58+134017.5	VLT	UBV	13.62	13.90	14.16	0.106	7473±171	4.00±0.25	−0.00±0.02	Am	22±4	2.0±0.6
	APO						7365±17	4.00±0.17	−0.72±0.15	Am	−10	1.3±0.3
PG2134+125[17]	VLT	UBV	17.02	17.45	17.08	0.131	>40000			CSPN	−55±9	2.2±0.8
BS17578−0016[18]	VLT	UBV	12.59	12.60	12.42	0.114	11772±280	3.83±0.10	0.00	AV	−35±5	3.6±0.5
	APO						12000±200	4.00±0.25	0.00±0.25	AV	−53	3.1±0.8
FWPeg[19]	VLT	Kuk	14.0			0.120	6500±250	2.50±0.50	−0.82±0.25	RR	−225±2[10]	3.8±0.8
2MASSJ213327.04+133026.7	VLT	UBV	14.98	15.02	14.90	0.111	11285±176	3.97±0.08	0.00	AV	−117±3	8.2±0.9
	APO						11500±200	4.25±0.25	0.00±0.25	AV	−118	7.2±0.4

Note. — 1: Source of spectroscopic data: APO=Apache Point Observatory; VLT=Very Large Telescope. 2: Source of photometry data: SDSS=Sloan Digital Sky Survey *ugr*; UBVS: SDSS photometry converted to UBV; UBV=our own UBV photometry; Str: Strömgren photometry; GSC: value from HST Guide Star Catalogue; Kuk: value from Kukarkin et al. (1970). 3: Magnitude – U,

B, V when Col. 3 has "UBV", SDSS r, g, u when Col. 3 has "SDSS", Strömgren y when Col. 3 has "Str", V magnitude from Kukarkin et al. (1970) when Col. 3 has "Kuk". 4: Derived effective temperature. 5: Derived gravity. 6: Derived abundance, relative to solar. 7: Spectral type: FHB=Field Horizontal Branch; RR=RR Lyrae; AV, FV=main sequence A or F star. 8: Derived stellar velocity; a note (10) indicates that there are multiple spectra and the velocity varies; the listed velocity then refers to the velocity of the star in the spectrum used to search for the interstellar absorption. Formal errors were not derived for velocities measured in the APO spectra – the pixels are about 50 $\mathrm{km\,s^{-1}}$ wide. 9: Derived distance; we prefer the distance derived using the VLT spectrum; for RR Lyrae stars we estimate the average magnitude, as explained in the text. 10: Stellar velocity is variable, the listed velocity is valid for the spectrum in which the interstellar lines are searched-for. 11: Temperature, gravity and distance from Moehler et al. (1990); star located at R.A.,Dec.=01:45:39.5 +15:04:42. 12: Redshift instead of velocity given for this QSO. 13: Too many stellar lines to reliably determine stellar velocity in low-resolution spectrum. 14: Star located at R.A.,Dec.=20:02:23.0,−00:32:09. 15: Star located at R.A.,Dec.=20:03:43.5,+00:53:38. 16: Star located at R.A.,Dec.=21:34:17.8,+13:38:04 17: Distance from Phillips (2004); this is the central star of the planetary nebula NGC 7094; star located at R.A.,Dec.=21:36:52.2,+13:35:00 18: Star located at R.A.,Dec.=21:34:45.4,+13:52:50 19: Star located at R.A.,Dec.=21:32:59.0,+12:52:24.

Table 2. Observational data

object	lon[1]	lat[1]	dist[2]	T^3_{exp}	Flux[4] (cont)	S/N[5] cont	Flux[6] (HVC)	S/N[7] (@v(HVC))
	[◦]	[◦]	[kpc]	[ks]	[f.u.]		[f.u.]	
(1)	(2)	(3)	(4)	(5)	(6)	(7)	(8)	(9)
Cohen Stream								
PG0142+148	141.87	−45.79	1.2±0.5	0.5	226	84	226	78
2MASSJ014825.88+132305.3	143.56	−47.19	2.1±1.3	1.0	137	83	128	80
2MASSJ021651.34+080150.2	156.43	−49.21	2.2±1.0	26.1[8]	4.2	85	3.5	79
2MASSJ021409.31+090105.3	154.81	−48.67	3.3±0.8	2.7[9]	190	84	132	55
2MASSJ014936.48+143914.6	143.36	−45.90	4.6±0.8	1.3	114	80	54	38
SDSSJ014843.61+130411.5	143.81	−47.47	5.0±1.2	3.0	45	96	15	42
SDSSJ020033.50+141154.0	147.14	−45.40	8.7±1.3	8.0[10]	22	43	11	28
SDSSJ015133.91+141105.2	144.23	−46.19	11.2±1.0	21.1[11]	17	99	13	69
SDSSJ015735.65+135254.2	146.36	−45.96	30.4±3.9	15.0[12]	4.0	37	4.0	36
SDSSJ014631.99+133506.3	142.83	−47.15	***	14.0	7.9	51	7.9	51
Complex GCP								
2MASSJ195741.61-004009.7	40.04	−15.01	0.7±0.6	8.4[13]	5.6	37	0.8	7.6
2MASSJ195927.29+000822.3	41.00	−15.02	1.1±0.5	1.6	38	52	17	35
2MASSJ195925.49-000519.1	40.79	−15.12	1.5±0.2	1.0	67	42	10	14
2MASSJ195912.00-002645.3	40.43	−15.24	1.8±0.3	1.0	84	55	22	25
2MASSJ195922.75+000300.0	40.91	−15.05	9.0±3.7	1.7	2.5	11	0.5	3.3
V1172Aql	40.74	−15.98	10.5±1.4	8.2[14]	11	52	7.6	52
2MASSJ195823.36-002719.0	40.32	−15.07	13.1±3.2	5.6[15]	3.9	24	0.5	4.6
V1084Aql	42.21	−15.60	14.5±1.3	11.0[16]	10	55	8.6	47
Cloud g1								
BS17578-0015	67.04	−27.17	1.2±0.3	0.5	2.5	77	1.9	70
2MASSJ213520.04+133045.0	67.12	−27.44	1.3±0.2	1.5	160	81	59	34
2MASSJ213451.58+134017.5	67.17	−27.25	2.0±0.6	2.6[17]	84	101	41	47
PG2134+125	66.78	−28.20	2.2±0.8	3.0	249	103	241	148
BS17578-0016	67.33	−27.10	3.6±0.5	0.5	658	106	603	101
FWPeg	66.15	−27.39	3.8±0.8	3.0[18]	67	71	64	73
2MASSJ213327.04+133026.7	66.78	−27.10	8.2±0.9	3.0[19]	40	73	40	91

Note. — 1: Galactic longitude and latitude of the star. 2: Distance estimate from Table 1. 3: Total exposure time, in kiloseconds (but see notes 8 to 19). 4: Stellar flux in the continuum in units of $10^{-16}\,\mathrm{erg\,cm^{-2}\,s^{-1}\,\AA^{-1}}$. 5: Signal-to-noise ratio in the continuum. 6: Stellar flux at the velocity of the high-velocity cloud in units of $10^{-16}\,\mathrm{erg\,cm^{-2}\,s^{-1}\,\AA^{-1}}$. 7: Signal-to-noise ratio at the velocity of the high-velocity cloud. 8: There are nine exposures – since the stellar velocity is constant they are all combined. 9: There are four exposures of this star, but for unknown reasons the flux in the second is much lower, so we exclude it. 10: There are three exposures; the stellar velocity is $-2\,\mathrm{km\,s^{-1}}$ in the first exposure, $-8\,\mathrm{km\,s^{-1}}$ in the second, $-29\,\mathrm{km\,s^{-1}}$ in the third – we only use the third exposure, as in exposures 1 and 2 a stellar line is shifted on top of the interstellar Ca II K line. 11: This star appears to be binary: in four of the seven exposures the stellar lines are at $-190\,\mathrm{km\,s^{-1}}$ (and we combine these four), but in the remaining three exposures the stellar line is much broader, appears to have two components, and is centered at -178, -138 and $-139\,\mathrm{km\,s^{-1}}$; it also confuses the interstellar Ca II K. 12: There are five exposures, with constant stellar velocity; however in the first exposure a spike (probably a cosmic ray) confuses the interstellar K line. 13: The first of the three exposures has lower stellar flux, so we don't use it. 14: The stellar velocity changed from -128 to -121 to $-115\,\mathrm{km\,s^{-1}}$ over the three contiguous hours of observing; since there are no stellar lines interfering with the interstellar Ca II K, we averaged the three exposures. 15: The two exposures of this star were combined. 16: The stellar velocity changed from -36 to -31 to $-26\,\mathrm{km\,s^{-1}}$ over the four contiguous hours of observing; since there are no stellar lines interfering with the interstellar Ca II K, we averaged these. 17: The two exposures of this star were combined. 18: The stellar velocity is $-225\,\mathrm{km\,s^{-1}}$ in the first exposure, $-170\,\mathrm{km\,s^{-1}}$ in the second; the wide stellar Ca II K line extends across the interstellar line in the second exposure, halving the flux, so we only use the first exposure. 19: The two exposures of this star were combined.

Table 3. Interstellar absorption line results

object	dist [kpc]	$v^1_{\rm LSR}$ [km s^{-1}]	log[2] N(HI)	W^3_{exp} [mÅ] (K)	W^3_{exp} [mÅ] (H)	W^3_{obs} [mÅ] (K)	W^3_{obs} [mÅ] (H)	logN^4 (K)	logN^4 (H)	A^5 [10^{-9}] (K)	A^5 [10^{-9}] (H)	U,L[6]
(1)	(2)	(3)	(4)	(5)	(6)	(7)	(8)	(9)	(10)	(11)	(12)	(13)
Cohen Stream (D=5.0–11.7 kpc)												
PG0142+148	1.2±0.5	−105	19.26	20	10	<7	<8	<10.88	<11.38	<4.2	<13.2	L
2MASSJ014825.88+132305.3	2.1±1.3	−106	19.41	22	11	<6	<15	<10.92	<11.38	<3.2	<9.3	L
2MASSJ021651.34+080150.2	2.2±1.0	−112	19.54	24	12	<10	<9	<11.05	<11.37	<3.2	<6.8	L
2MASSJ021409.31+090105.3	3.3±0.8	−110	19.08	19	9							
2MASSJ014936.48+143914.6	4.6±0.8	−106	19.30	21	10	<9	<11	<11.02	<11.48	<5.2	<15	L
SDSSJ014843.61+130411.5	5.0±1.2	−103	19.18	19	10	<10	<10	<11.08	<11.48	<7.9	<20	
SDSSJ020033.50+141154.0	8.7±1.3	−108	18.94	17	9	<17	<19	<11.28	<11.72	<22	<60	
SDSSJ015133.91+141105.2	11.2±1.0	−104	19.26	20	10	17±3	<28	11.33±0.07	<11.54	11.7±2.9	<19	U
SDSSJ015735.65+135254.2	30.4±3.9	−104	18.90	17	8	10±3	<18	11.06±0.20	<11.63	14.5±7.6	<54	U
SDSSJ014631.99+133506.3	***	−105	19.51	23	11	17±3	11±3	11.31±0.09	11.41±0.12	6.3±1.7	7.9±2.5	U
IV-South (D=1.0–2.7 kpc)												
PG0142+148	1.2±0.5	−51	19.54	28	14	<7	<8	<10.94	<11.25	<2.5	<5.1	L
2MASSJ014825.88+132305.3	2.1±1.3	−41	19.11	23	11	25±2		11.50±0.04		24±5		U
2MASSJ021651.34+080150.2	2.2±1.0	−75	18.93	21	10							
2MASSJ021409.31+090105.3	3.3±0.8	−63	18.77	19	9							
2MASSJ014936.48+143914.6	4.6±0.8	−51	19.49	27	14	26±4	<14	11.50±0.06	<11.50	10.2±2.5	<10.2	U
SDSSJ014843.61+130411.5	5.0±1.2	−35	19.18	23	12	<12	<10	<11.02	<11.49	<6.9	<20	
SDSSJ020033.50+141154.0	8.7±1.3	−46	18.86	20	10							
SDSSJ015133.91+141105.2	11.2±1.0	−49	19.23	24	12	16±3	26±2	11.29±0.08	11.50±0.04	11.5±3.0	19±4	U
SDSSJ015735.65+135254.2	30.4±3.9	−48	18.95	21	10	22±3	<21	11.42±0.10	<11.80	30±9	<71	U
SDSSJ014631.99+133506.3	***	−43	19.20	24	12	30±3	19±3	11.55±0.06	11.66±0.10	22±5	29±8	U
Complex GCP (D=9.8-15.1 kpc)												

Table 3—Continued

object	dist [kpc]	$v^1_{\rm LSR}$ [km s^{-1}]	log^2 N(HI)	W$^3_{exp}$ [mÅ] (K)	W$^3_{exp}$ [mÅ] (H)	W$^3_{obs}$ [mÅ] (K)	W$^3_{obs}$ [mÅ] (H)	logN^4 (K)	logN^4 (H)	A^5 [10^{-9}] (K)	A^5 [10^{-9}] (H)	U,L^6
(1)	(2)	(3)	(4)	(5)	(6)	(7)	(8)	(9)	(10)	(11)	(12)	(13)
2MASSJ195741.61-004009.7	0.7±0.6	89	20.16	61	32	<43	<40	<11.70	<12.19	<3.5	<10.7	
2MASSJ195927.29+000822.3	1.1±0.5	93	20.19	64	33	<13	<18	<11.17	<11.61	<1.0	<2.6	L
2MASSJ195925.49-000519.1	1.5±0.2	93	20.15	62	32	<28		<11.58		<2.7		
2MASSJ195912.00-002645.3	1.8±0.3	93	20.13	62	32	<15	<16	<11.18	<11.49	<1.1	<2.3	L
2MASSJ195922.75+000300.0	9.0±3.7	93	20.17	63	32	<124	<158	<12.36	<12.54	<16	<23	
V1172Aql	10.5±1.4	94	20.03	59	30	<11	<13	<11.13	<11.56	<1.3	<3.4	L
2MASSJ195823.36-002719.0	13.1±3.2	90	20.12	61	31	<68	<57	<12.09	<12.25	<9.3	<13.5	
V1084Aql	14.5±1.3	91	20.08	61	31	51±3	37±10	11.82±0.02	11.96±0.13	5.5±1.1	7.6±2.4	U
Cloud g1 (D=1.8-3.8 kpc)												
BS17578-0015	1.2±0.3	71	19.04	74	39	<5	<8	<10.73	<11.02	<4.9	<9.5	L
2MASSJ213520.04+133045.0	1.3±0.2	71	19.04	75	39	<8	<11	<10.99	<11.59	<8.9	<36	L
2MASSJ213451.58+134017.5	2.0±0.6	71	18.95	72	38	<8	<10	<10.94	<11.35	<9.8	<25	L
PG2134+125	2.2±0.8	70	18.92	69	37	<4	<5	<10.66	<11.00	<5.5	<12.0	L
BS17578-0016	3.6±0.5	67	18.51	55	29	30±2	14±3	11.56±0.03	11.52±0.14	112±24	102±35	U
		80	18.08	42	23	44±2	31±3	11.74±0.02	11.87±0.04	457±94	617±137	U
FWPeg	3.8±0.8	67	19.23	82	43	127±4	73±4	12.25±0.01	12.26±0.03	105±21	107±23	U
2MASSJ213327.04+133026.7	8.2±0.9	72	19.11	77	41	66±3	27±9	11.92±0.02	11.88±0.14	65±13	59±20	U
Low-velocity gas near CS												
PG0142+148	1.2±0.5	−3	20.56	203	112	94±2	65±4	12.12±0.01	12.22±0.03	3.6±0.7	4.6±1.0	U
2MASSJ014825.88+132305.3	2.1±1.3	−6	20.65	208	115	98±3	64±7	12.16±0.01	12.23±0.05	3.2±0.6	3.8±0.9	U
2MASSJ021651.34+080150.2	2.2±1.0	−12	20.81	226	127	115±6	<11	12.24±0.02	<12.23	2.7±0.6	<2.6	U
2MASSJ021409.31+090105.3	3.3±0.8	−13	20.75	213	119							
2MASSJ014936.48+143914.6	4.6±0.8	−4	20.59	206	114	124±5	52±7	12.26±0.02	12.13±0.07	4.7±1.0	3.5±0.9	U

Table 3—Continued

object	dist [kpc]	$v^1_{\rm LSR}$ [km s^{-1}]	log^2 N(HI)	W$^3_{exp}$ [mÅ] (K)	W$^3_{exp}$ [mÅ] (H)	W$^3_{obs}$ [mÅ] (K)	W$^3_{obs}$ [mÅ] (H)	logN^4 (K)	logN^4 (H)	A^5 [10^{-9}] (K)	A^5 [10^{-9}] (H)	U,L^6
(1)	(2)	(3)	(4)	(5)	(6)	(7)	(8)	(9)	(10)	(11)	(12)	(13)
SDSSJ014843.61+130411.5	5.0±1.2	−5	20.69	216	121	120±5	78±4	12.26±0.02	12.31±0.04	3.7±0.8	4.2±0.9	U
SDSSJ020033.50+141154.0	8.7±1.3	−4	20.68	212	118	120±18	102±16	12.30±0.08	12.49±0.06	4.2±1.1	6.5±1.6	U
SDSSJ015133.91+141105.2	11.2±1.0	−6	20.62	204	113	183±3	123±7	12.57±0.01	12.61±0.03	8.9±1.8	9.8±2.0	U
SDSSJ015735.65+135254.2	30.4±3.9	−6	20.66	213	118							
SDSSJ014631.99+133506.3	***	−4	20.47	193	106	155±4	76±4	12.35±0.02	12.30±0.03	7.6±1.5	6.8±1.5	U
Low-velocity gas near GCP												
2MASSJ195741.61-004009.7	0.7±0.6	32	20.47	177	101	181±16	<74	12.50±0.06	<12.35	10.7±2.5	<7.6	U
2MASSJ195927.29+000822.3	1.1±0.5	30	20.43	176	101	186±6	89±9	12.52±0.02	12.41±0.05	12.3±2.5	9.5±2.1	U
2MASSJ195925.49-000519.1	1.5±0.2	32	20.40	176	101							
2MASSJ195912.00-002645.3	1.8±0.3	35	20.37	170	97	124±10	84±9	12.24±0.05	12.35±0.05	7.4±1.7	9.5±2.2	U
2MASSJ195922.75+000300.0	9.0±3.7	32	20.42	174	99	366±46	<222	12.91±0.15	<12.84	31±16	<26	U
V1172Aql	10.5±1.4	27	20.41	175	100	230±4	152±6	12.58±0.01	12.67±0.02	14.8±3.0	18±4	U
2MASSJ195823.36-002719.0	13.1±3.2	32	20.40	175	100	303±24	250±22	12.87±0.13	12.96±0.07	30±12	36±9	U
V1084Aql	14.5±1.3	32	20.33	167	95	240±3	130±11	12.65±0.01	12.57±0.04	21±4	17±4	U
Low-velocity gas near GCP												
2MASSJ195741.61-004009.7	0.7±0.6	0	20.82	200	117	118±11	94±13	12.31±0.06	12.46±0.06	3.1±0.7	4.4±1.1	U
2MASSJ195927.29+000822.3	1.1±0.5	0	20.85	202	118	213±5	121±7	12.61±0.02	12.56±0.03	5.8±1.2	5.1±1.1	U
2MASSJ195925.49-000519.1	1.5±0.2	0	20.82	202	118							
2MASSJ195912.00-002645.3	1.8±0.3	0	20.79	199	116	154±9	111±8	12.42±0.01	12.50±0.03	4.3±0.9	5.1±1.1	U
2MASSJ195922.75+000300.0	9.0±3.7	0	20.84	207	122	193±43	<160	12.60±0.31	<12.71	5.8±3.2	<7.4	U
V1172Aql	10.5±1.4	1	20.78	196	114	128±5	182±5	12.32±0.02	12.78±0.02	3.5±0.7	10.0±2.0	U
2MASSJ195823.36-002719.0	13.1±3.2	0	20.80	203	119	200±18	150±17	12.67±0.16	12.73±0.07	7.4±3.5	8.5±2.2	U
V1084Aql	14.5±1.3	1	20.82	199	117	248±4	181±9	12.67±0.01	12.74±0.02	7.1±1.4	8.3±1.7	U

Table 3—Continued

object	dist [kpc]	$v^1_{\rm LSR}$ [km s^{-1}]	log^2 N(HI)	W$^3_{exp}$ [mÅ] (K)	W$^3_{exp}$ [mÅ] (H)	W$^3_{obs}$ [mÅ] (K)	W$^3_{obs}$ [mÅ] (H)	logN^4 (K)	logN^4 (H)	A^5 [10^{-9}] (K)	A^5 [10^{-9}] (H)	U,L^6
(1)	(2)	(3)	(4)	(5)	(6)	(7)	(8)	(9)	(10)	(11)	(12)	(13)
Low-velocity gas near g1												
BS17578-0015	1.2±0.3	2	20.82	221	123	115±3	74±3	12.25±0.01	12.30±0.02	2.7±0.5	3.0±0.6	U
2MASSJ213520.04+133045.0	1.3±0.2	4	20.84	228	128	235±3	176±3	12.66±0.01	12.74±0.01	6.6±1.3	7.9±1.6	U
2MASSJ213451.58+134017.5	2.0±0.6	4	20.82	220	123	155±9	108±6	12.39±0.02	12.48±0.02	3.7±0.8	4.6±0.9	U
PG2134+125	2.2±0.8	1	20.84	230	129	178±2	107±2	12.46±0.00	12.47±0.01	4.2±0.8	4.3±0.9	U
BS17578-0016	3.6±0.5	2	20.79	219	123	216±2	132±3	12.58±0.00	12.58±0.01	6.2±1.2	6.2±1.3	U
FWPeg	3.8±0.8	3	20.79	197	116	287±3	197±5	12.72±0.01	12.78±0.01	8.5±1.7	9.8±2.0	U
2MASSJ213327.04+133026.7	8.2±0.9	2	20.80	226	127	260±2		12.65±0.00		7.1±1.4		U

Note. — 1: Velocity of HVC or IVC in the direction of the star. 2: Logarithm of 21-cm H I column density in the high-velocity cloud. 3: Expected and observed equivalent width of the high-velocity cloud Ca II absorption. 4: Logarithm of integrated apparent Ca II column density (in cm^{-2}) based on the K (Col. 9) or H (Col. 10) line profile. 5: Ca II/H I ratio in units of 10^{-9}, using N(K) (Col. 11) or N(H) (Col. 12); the error includes a 20% error in the H I column density. 6: Conclusion drawn concerning HVC or IVC distance from this sightline: U means upper limit, L means lower limit, no entry is given if the non-detection is not significant.

Table 4. Summary of cloud parameters

Quantity	Cohen Stream	Perseus Arm IVC	Complex GCP	Cloud g1
Distance [kpc]	5.0–11.7	1.0–2.7	9.8–15.1	1.8–3.8
Radius [kpc]	11.5–15.7	9.1–10.2	6.2–9.7	8.0–7.8
Height [kpc]	3.7–8.6	0.7–1.8	2.5–3.9	0.8–1.7
Size [deg]	1×12	3×8	2×8	2×2
H I parameters				
N(HI) (peak) [cm^{-2}]	3.5×10^{19}	6.0×10^{19}	17.0×10^{19}	2.5×10^{19}
Lx [pc]	90–200	50–140	340–530	60–130
Ly [pc]	1000–2500	100–400	1400–2100	60–130
n(HI) [cm^{-3}]	0.13–0.06	0.37–0.14	0.16–0.10	0.13–0.06
M(HI) [M$_\odot$]	$0.73–4.02\times10^{5}$	$1.86–13.57\times10^{4}$	$0.68–1.60\times10^{6}$	$0.09–0.41\times10^{4}$
M(HI) [M$_\odot$ yr^{-1}]	$2.0–4.7\times10^{-3}$	$16.0–43.2\times10^{-4}$	$6.4–9.8\times10^{-3}$	$0.8–1.6\times10^{-4}$
H$^+$ parameters assuming H$^+$ has same pathlength as H I				
I(Hα) [R]	0.07±0.01	<0.15	0.27±0.03	1.1±0.2
n(H$^+$) [cm^{-3}]	0.04–0.03	<0.08–<0.05	0.04–0.03	0.20–0.14
N(H$^+$) [cm^{-2}]	$1.1–1.7\times10^{19}$	$<1.3–<2.1\times10^{19}$	$4.4–5.5\times10^{19}$	$3.8–5.6\times10^{19}$
M(H$^+$) [M$_\odot$]	$0.7–5.9\times10^{5}$	$<0.7–<8.5\times10^{4}$	$0.6–1.9\times10^{6}$	$0.4–2.3\times10^{4}$
M(H$^+$) [M$_\odot$ yr^{-1}]	$1.9–6.8\times10^{-3}$	$<6.0–<26.8\times10^{-4}$	$6.7–12.8\times10^{-3}$	$3.0–9.2\times10^{-4}$
H$^+$ parameters assuming H$^+$ has same volume density as H I				
L [pc]	9–51	<2–<18	23–55	148–660
n(H$^+$) [cm^{-3}]	0.13–0.06	<0.37–<0.14	0.16–0.10	0.13–0.06
N(H$^+$) [cm^{-2}]	$0.4–0.9\times10^{19}$	$<0.3–<0.8\times10^{19}$	$1.2–1.8\times10^{19}$	$5.9–12.4\times10^{19}$
M(H$^+$) [M$_\odot$]	$0.2–2.9\times10^{5}$	$<0.2–<3.0\times10^{4}$	$0.2–0.6\times10^{6}$	$0.6–5.2\times10^{4}$
M(H$^+$) [M$_\odot$ yr^{-1}]	$0.6–3.4\times10^{-3}$	$<1.3–<9.5\times10^{-4}$	$1.7–4.1\times10^{-3}$	$4.6–20.5\times10^{-4}$

Note. — The mass flows are for infall in the case of the Cohen Stream and the Perseus Arm IVC, but they represent outflows for complex GCP and cloud g1.

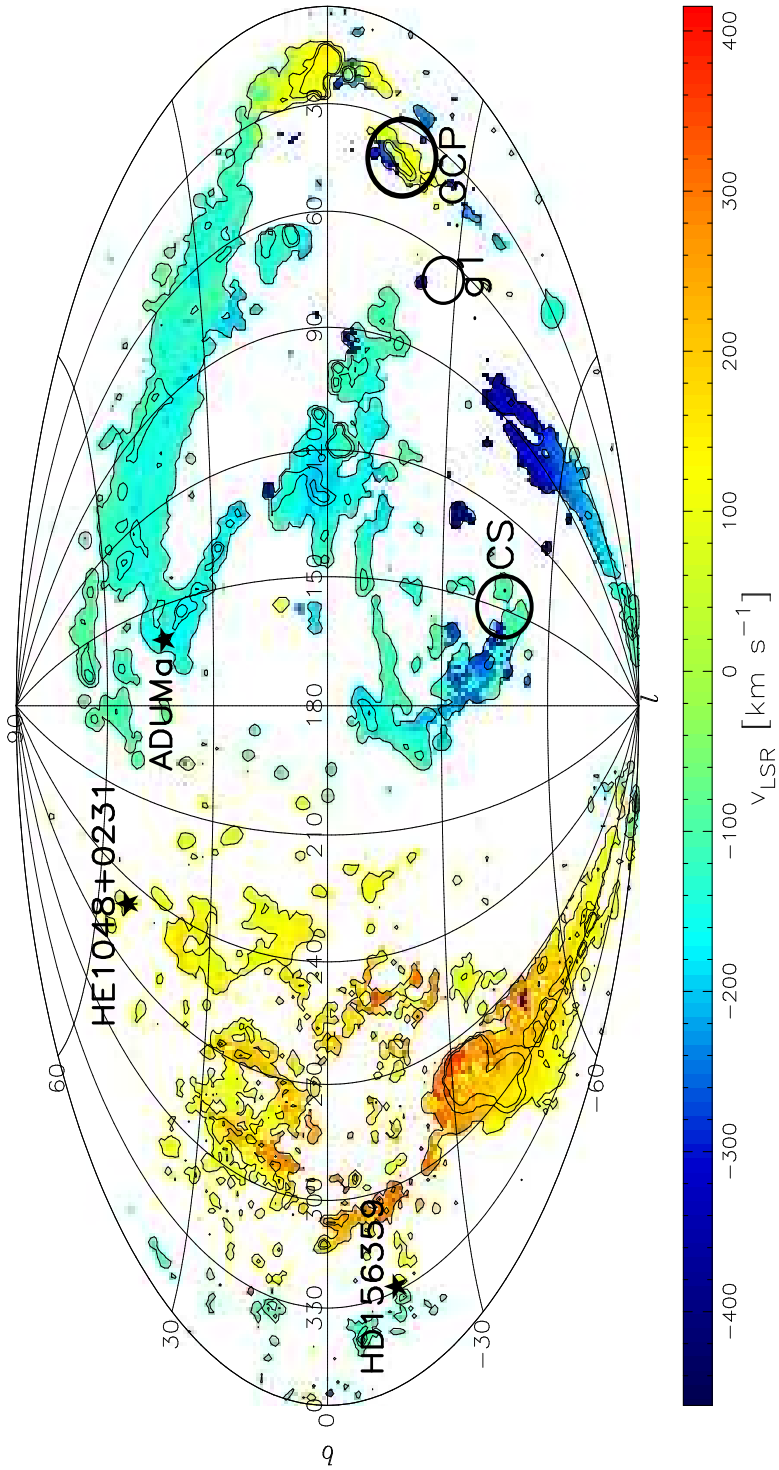

Fig. 1.— All-sky map of the high-velocity cloud sky, based on the data of Hulsbosch & Wakker (1988) and Morras et al. (2000). Colors represent LSR velocities, as coded in the wedge. Contour levels are at brightness temperatures of 0.05, 0.25, 0.5 and 1 K. The positions of the clouds discussed in this paper are shown by the thick-rimmed circles. Note that cloud g1 does not show up in this map because its velocity (+70 km s^{-1}) falls outside the velocity range covered by Hulsbosch & Wakker (1988). Also shown are the locations of the three stars toward which high-velocity absorption was previously detected.

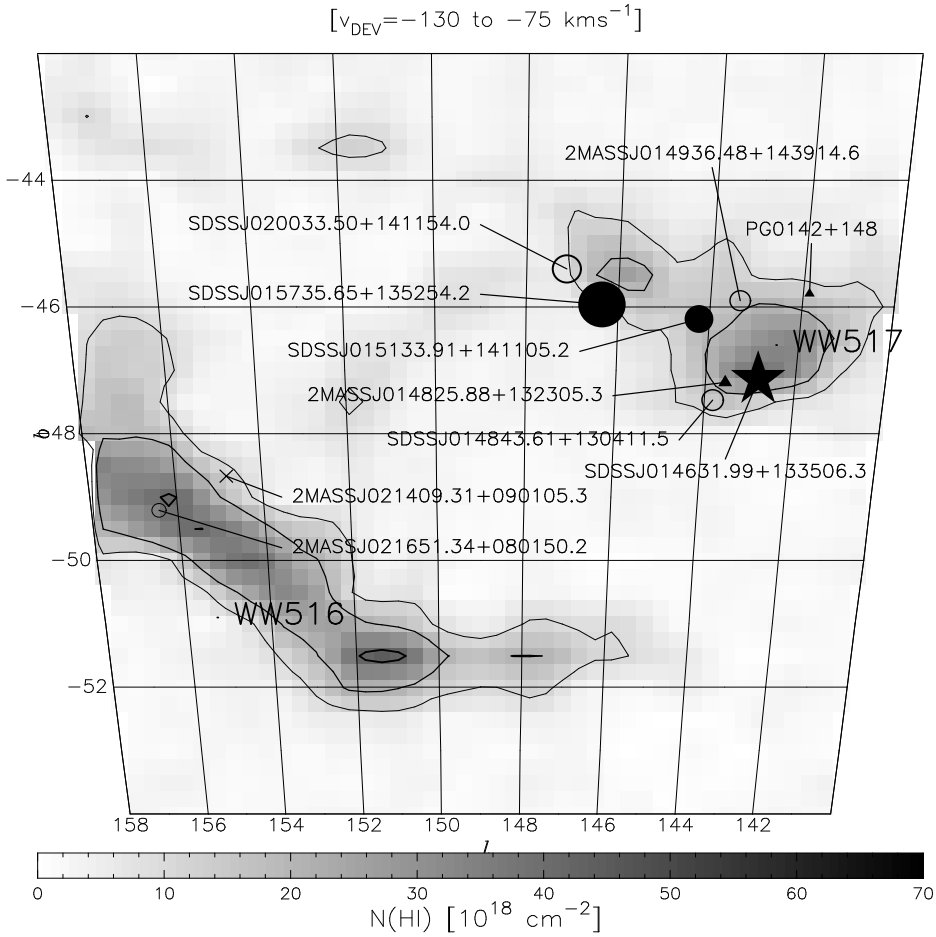

Fig. 2.— Map of the column density of the Cohen Stream, integrating the LAB data of Kalberla et al. (2005) between $v_{\rm LSR}$=−130 km s^{-1} and $v_{\rm LSR}$=−80 km s^{-1}. Contours are at column densities of 1, 2 and 4×10^{19} cm^{-2}. The locations of the background stars are overlaid. The size (i.e. area) of the symbols is proportional to the distance of the star. Closed circles are for directions where the HVC is detected in absorption. Closed triangles are for significant non-detections. Open circles are for non-detections that do not allow a conclusion concerning the HVC's distance. Crosses are for stars where the interstellar absorption is too blended with stellar lines. The QSO is shown by an five-pointed star instead of a closed circle.

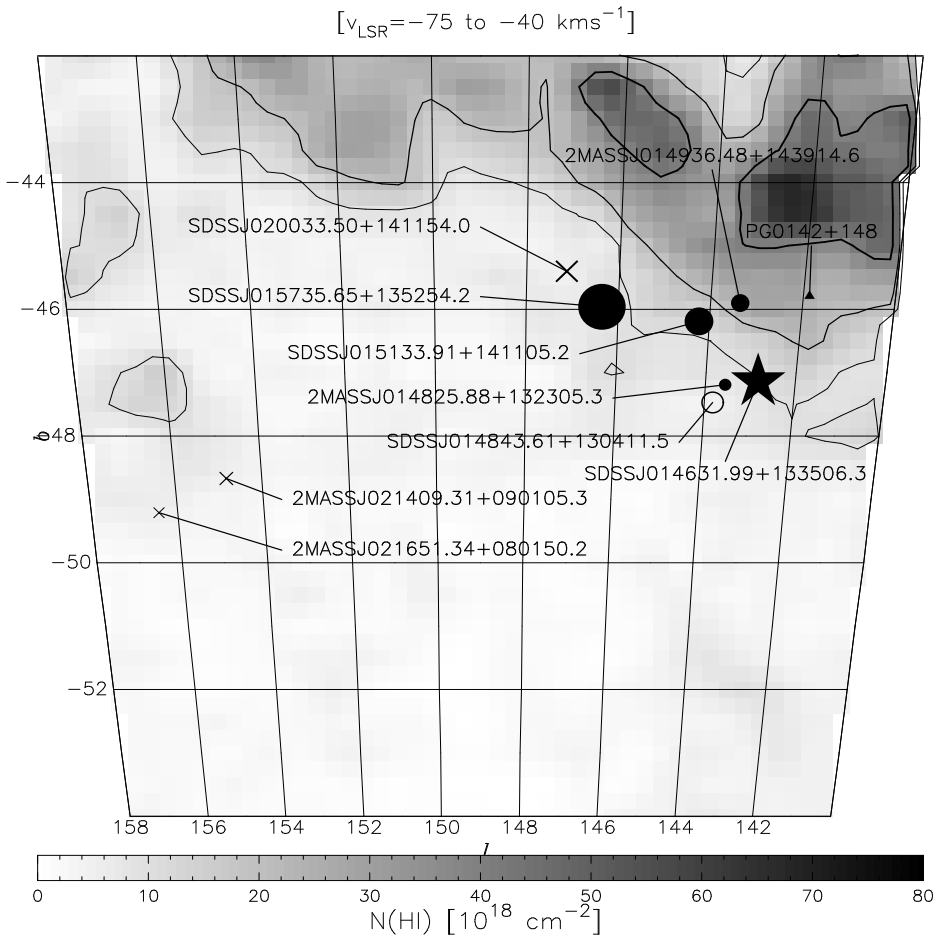

Fig. 3.— Map of the column density of the IVC in the Cohen Stream field, gas probably associated with the high-z extension of the Perseus Arm, integrating the LAB data of Kalberla et al. (2005) between $v_{\rm LSR}$=−80 km s^{-1} and $v_{\rm LSR}$=−30 km s^{-1}. Contours are at column densities of 1, 2 and 4×10^{19} cm^{-2}. The locations of the background stars are overlaid. Symbols are as for Fig. 2.

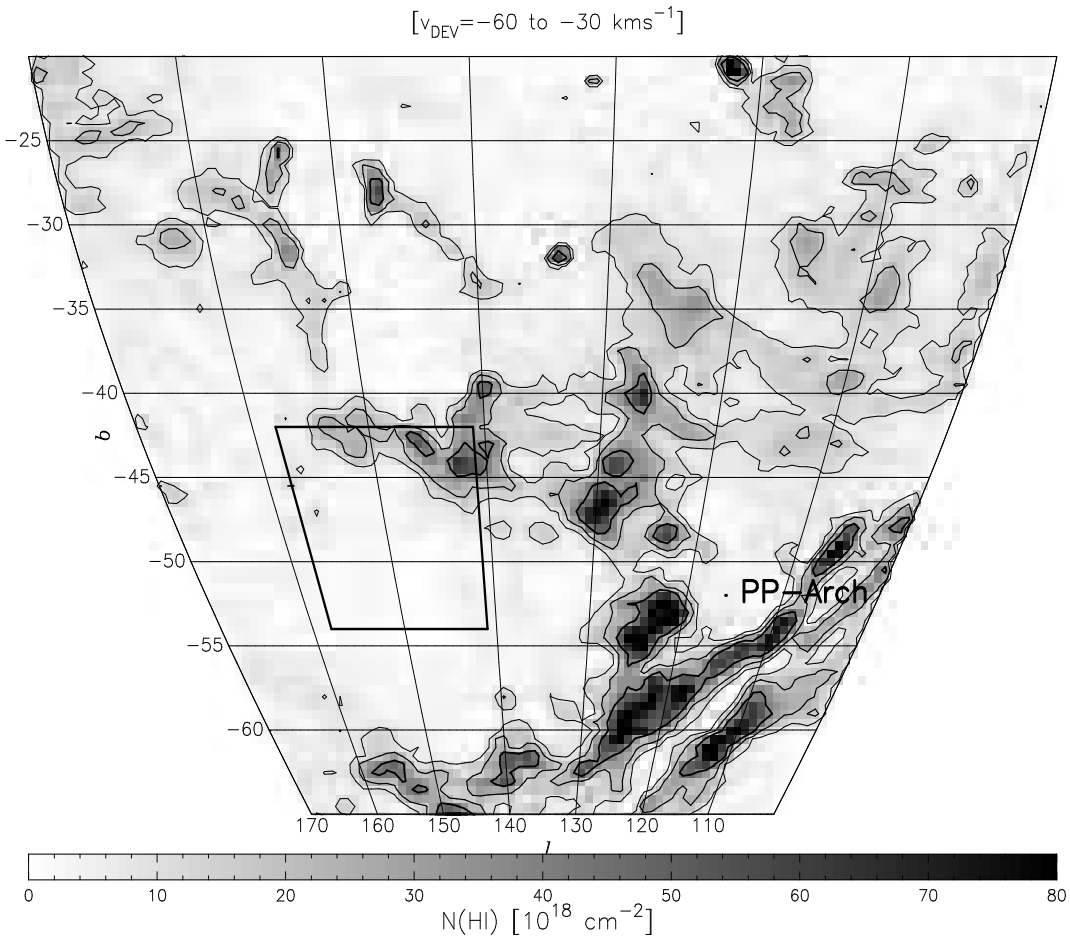

Fig. 4.— Map of the column density of the intermediate-velocity gas in a large region to the south of the Perseus Arm. This map represents the H I column density in the LAB data of Kalberla et al. (2005) integrated between deviation velocities $v_{\rm DEV}$=−60 km s^{-1} and $v_{\rm DEV}$=−30 km s^{-1}. Contours are at column densities of 1, 2 and 4×10^{19} cm^{-2}. The box outlines the region shown in Figs. 2 and 3.

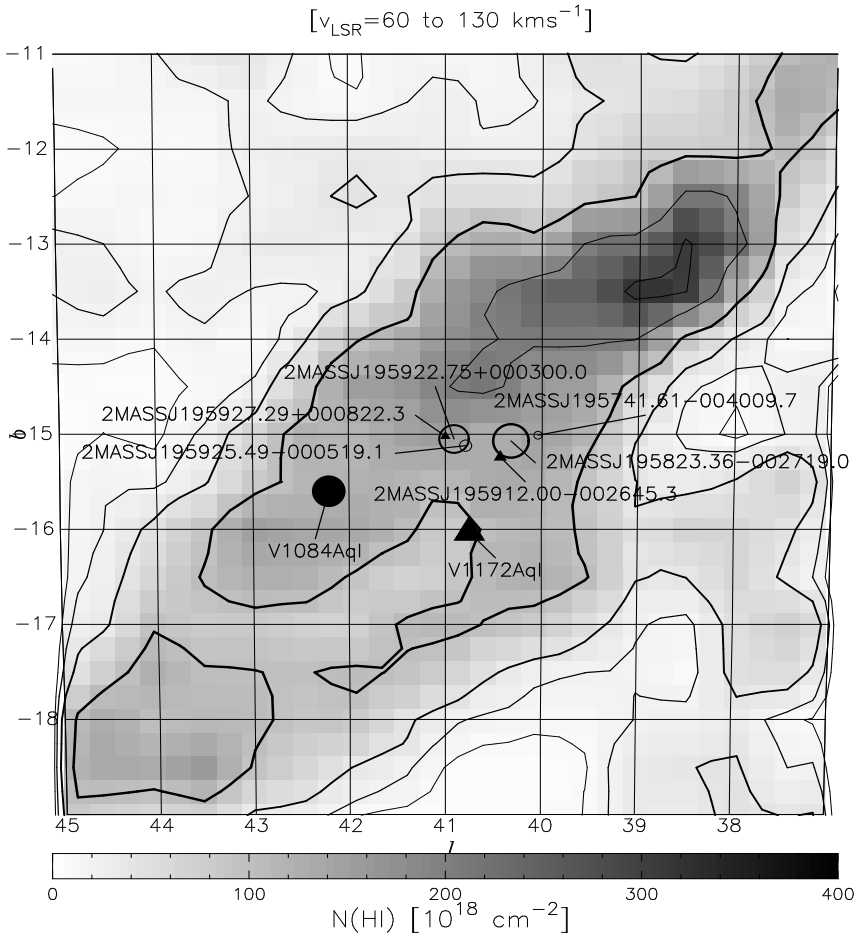

Fig. 5.— Map of the column density of complex GCP, integrating the LAB data of Kalberla et al. (2005) between $v_{\rm LSR}$=+60 km s^{-1} and $v_{\rm LSR}$=+130 km s^{-1}. Contours are at N(H I)= 1, 2, 4, 10, 20 and 30×10^{19} cm^{-2}. Symbols are as for Fig. 2.

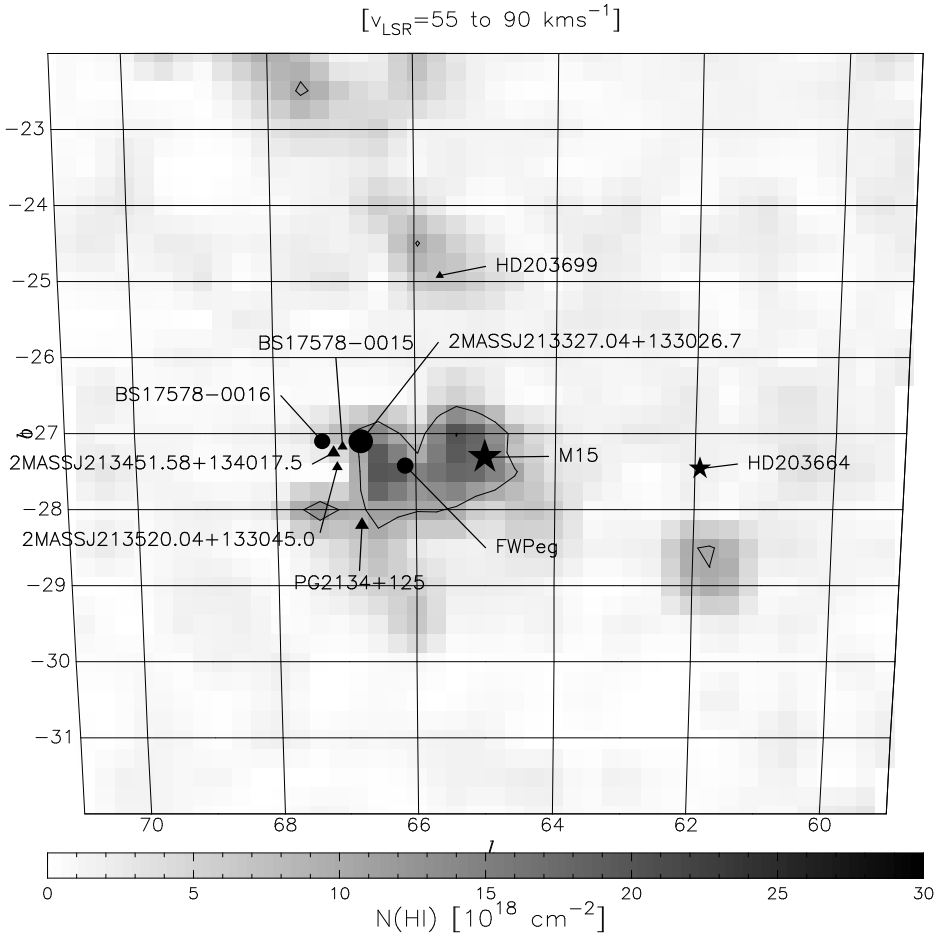

Fig. 6.— Map of the column density of the g1 cloud, integrating the LAB data of Kalberla et al. (2005) between $v_{\rm LSR}$=+55 km s^{-1} and $v_{\rm LSR}$=+90 km s^{-1}. Contours are at 1, 2, and 4×10^{19} cm^{-2}. Symbols are as for Fig. 2.

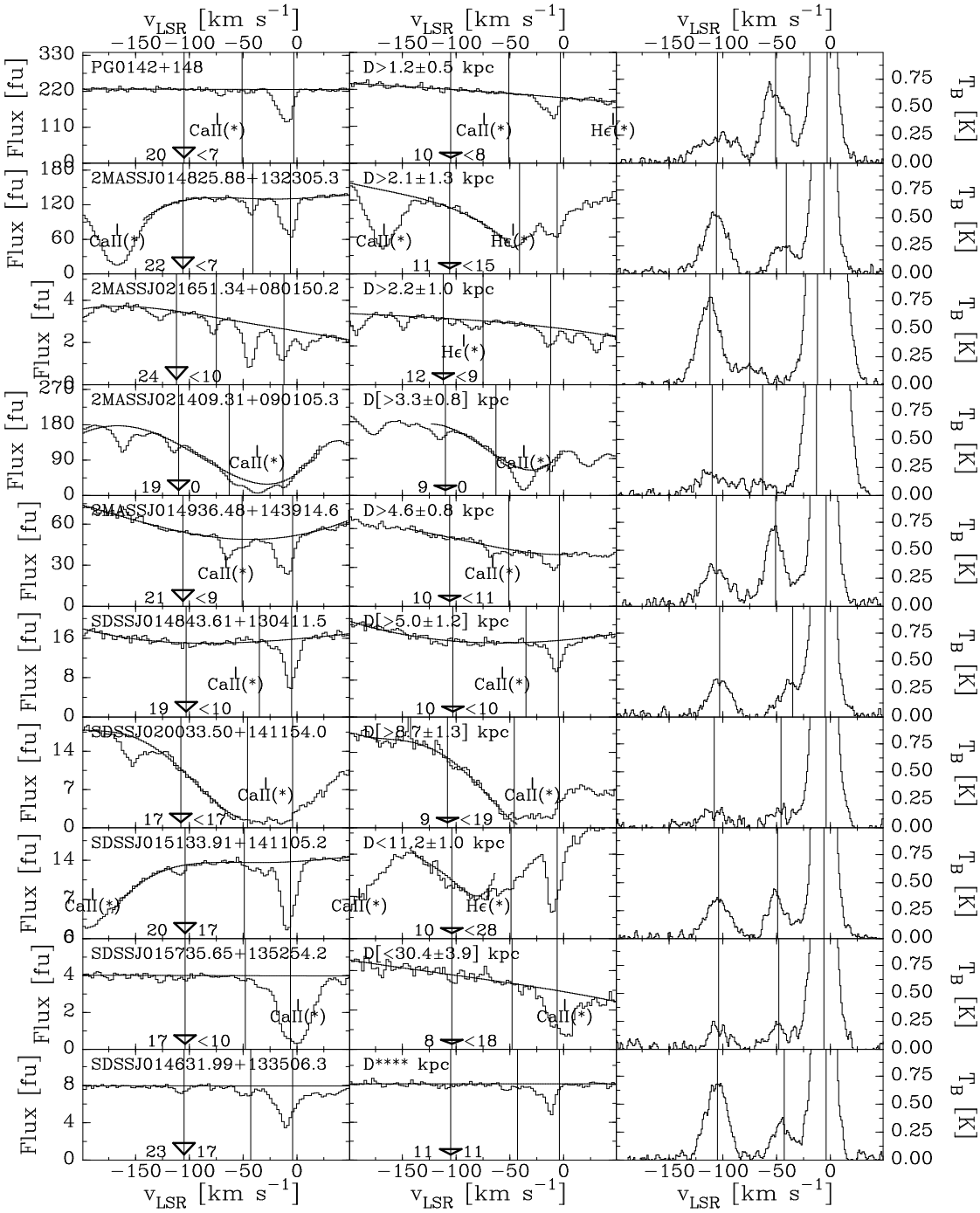

Fig. 7.— Spectra for stars toward the Cohen Stream. Flux units (f.u.) are 10^{-16} erg cm^{-2} s^{-1} Å^{-1}. Left column: Ca II K spectra (histograms) and continuum fits (solid curves); middle column: Ca II H spectra and continua (note that the left flux scale is valid only for Ca II K); right column: H I-21 cm spectra. One star per row, with the name and distance given in the top left corner of the K and H panels. Distances are preceded by "$>$" for lower limits, by "$<$" for upper limits. Distances in brackets show that the detection limit is worse than the expected equivalent width, or there are too many stellar lines. Labels (Ca II(*) and Hϵ(*)) show the positions of stellar absorption lines. Vertical lines give the velocities of the H I components. Triangles and numbers in each Ca II panel give the shape of the expected absorption line, the expected equivalent width, and the 3σ detection limit or the detected equivalent width (a "0" means there is a blended stellar line).

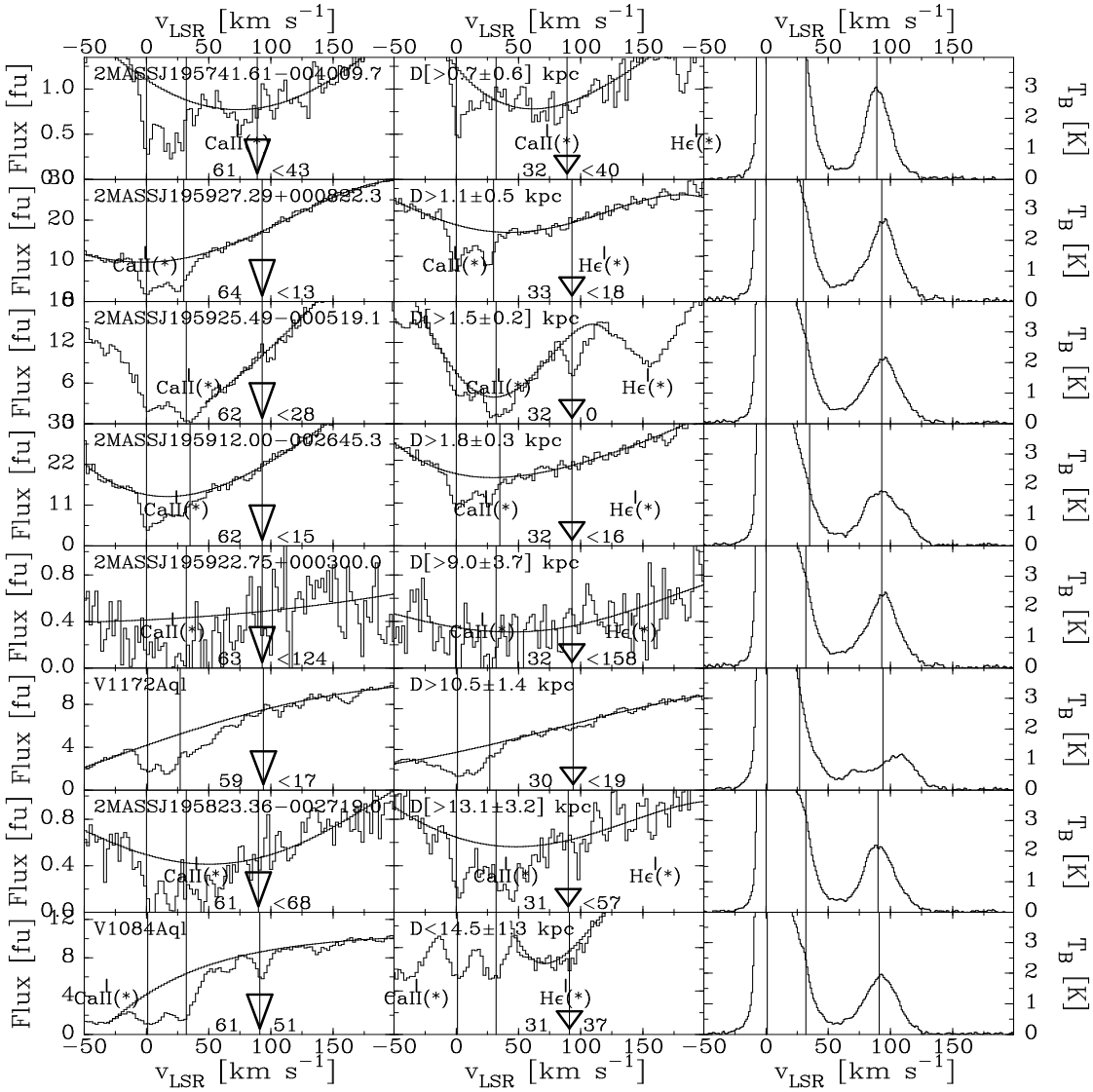

Fig. 8.— Same as Fig. 7, except for complex GCP.

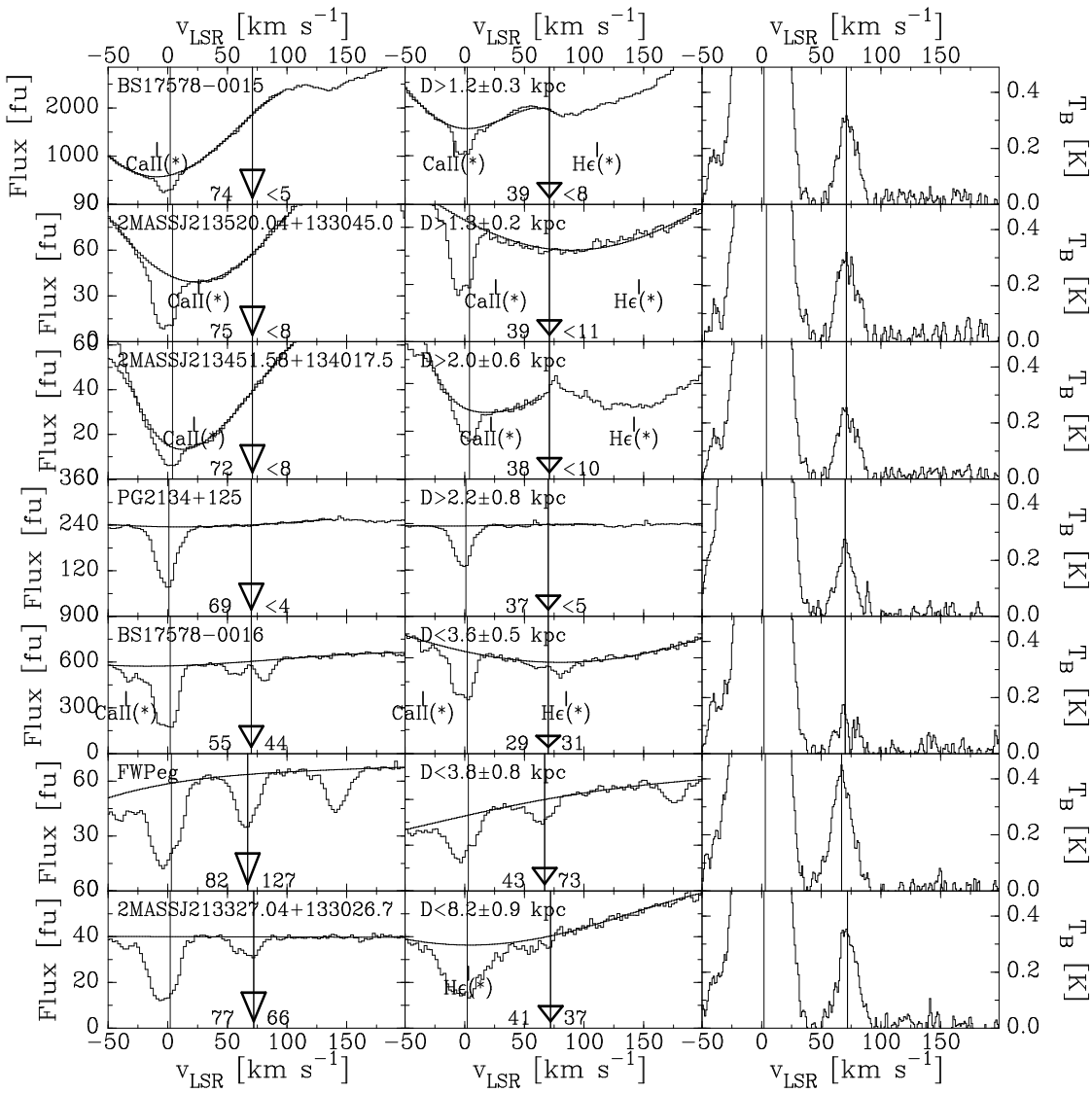

Fig. 9.— Same as Fig. 7, except for cloud g1.